JOURNAL OF GEOPHYSICAL RESEARCH, VOL. 112, B03S09, doi:10.1029/2006JB004362, 2007

Click Here for Full Article

Mechanisms of active folding of the landscape (southern Tian Shan, China)

Aurélia Hubert-Ferrari,[1,2] John Suppe,[3] Ramon Gonzalez-Mieres,[3] and Xin Wang[4]

Received 23 February 2006; revised 2 October 2006; accepted 28 November 2006; published 29 March 2007.

[1] We explore the kinematic mechanisms of active large-scale folding, based on analysis of two adjacent major anticlines in Tian Shan (central Asia) that share an acceleration of shortening rate leading to topographic emergence and folded geomorphic surfaces. Their folding mechanisms are fundamentally different. Yakeng anticline is a gentle pure shear detachment fold with 1200 m of shortening and a well-constrained history of growth beginning at 5.5 Ma with an order-of-magnitude increase in shortening rate from 0.16 to ~1.2–1.6 mm/yr at ~0.16–0.21 Ma. The shape of the deformed topographic surface and of subsurface horizons deposited during deformation is a linearly proportional image at reduced amplitude of the deeper structure, which shows that instantaneous uplift rates have been pointwise linearly proportional to the current finite fold amplitude. In contrast, Quilitak anticline is a complex fault bend fold with uplift rates proportional to the sine of the fault dip, showing discontinuities in uplift rate across active axial surfaces. The 10- to 20-km-wide anticline is topographically emergent only in a central 5- to 7-km-wide mountainous uplift, the abrupt southern edge of which is marked by ~600- to 700-m-high triangular facets that result from active folding of a pediment across an active axial surface. The giant facets are shown to form by kink band migration and record postemergence deformation since an order-of-magnitude acceleration in shortening rate from ~0.6 to ~4–5 mm/yr, apparently contemporaneous with Yakeng. Sections logged across the active ~115-m-wide hinge zone show that recent strata provide a bed-by-bed record of fold scarp growth, which is quantitatively deciphered by fitting bed shapes to a finite width kink band migration model.

Citation: Hubert-Ferrari, A., J. Suppe, R. Gonzalez-Mieres, and X. Wang (2007), Mechanisms of active folding of the landscape (southern Tian Shan, China), *J. Geophys. Res.*, *112*, B03S09, doi:10.1029/2006JB004362.

1. Introduction

[2] An unfortunate reality in tectonic geomorphology and coseismic geodesy has been the normal lack of strong constraints on the associated subsurface structure, making it difficult to form relationships between deformation of the land surface and actual underlying processes. Typically the subsurface structure in areas of active tectonics is known in only rather general terms, although there are some notable exceptions [e.g., *Medwedeff*, 1992; *Mueller and Tailing*, 1997; *Shaw et al.*, 2002; *Ishiyama et al.*, 2004]. Here we take advantage of an unusual coincidence of excellent subsurface data and well-preserved geomorphic expression for the active Yakeng and Quilitak anticlines of the southern Tian Shan thrust belt of western China. These two folds display fundamentally different folding mechanisms and associated surface expressions: (1) The Yakeng anticline is a detachment fold with uplift displaying progressive large-scale rotation of fold limbs and incremental uplift that is linearly proportional to total uplift. (2) In contrast, the Quilitak anticline is a complex fault bend fold involving kink band migration defined by large-scale fold scarps that mark localized discontinuities in uplift rate across the structure, with little evidence of rotation of fold limbs. Making use of these examples, we present evidence for a variety of little recognized but probably widespread active tectonic phenomena, applying some new techniques of analysis and modeling.

[3] A number of simple kinematic models have been developed to describe the diverse folding mechanisms that have been recognized in thrust belts, including detachment folding, fault bend folding, and fault propagation folding models [e.g., *Erslev*, 1991; *Epard and Groshong*, 1995; *Poblet and McClay*, 1996; *Suppe*, 1983; *Suppe et al.*, 1992, 2004; *Hardy and Ford*, 1997; *Allmendinger*, 1998]. These models make very different predictions for the distribution of instantaneous uplift relative to total uplift. If these models are reasonable approximations to the kinematics of actual structures, then we expect to see a rich variety of contrasting geomorphic expressions of the underlying active folding mechanisms. Figure 1 shows several of these models in their most elemental form.

[1] Institut de Géologie, Université de Neuchâtel, Neuchâtel, Switzerland.
[2] Now at Royal Observatory of Belgium, Brussels, Belgium.
[3] Department of Geosciences, Princeton University, Princeton, New Jersey, USA.
[4] Geosciences Department, Zhejiang University, Hangzhou, China.

Copyright 2007 by the American Geophysical Union.
0148-0227/07/2006JB004362$09.00

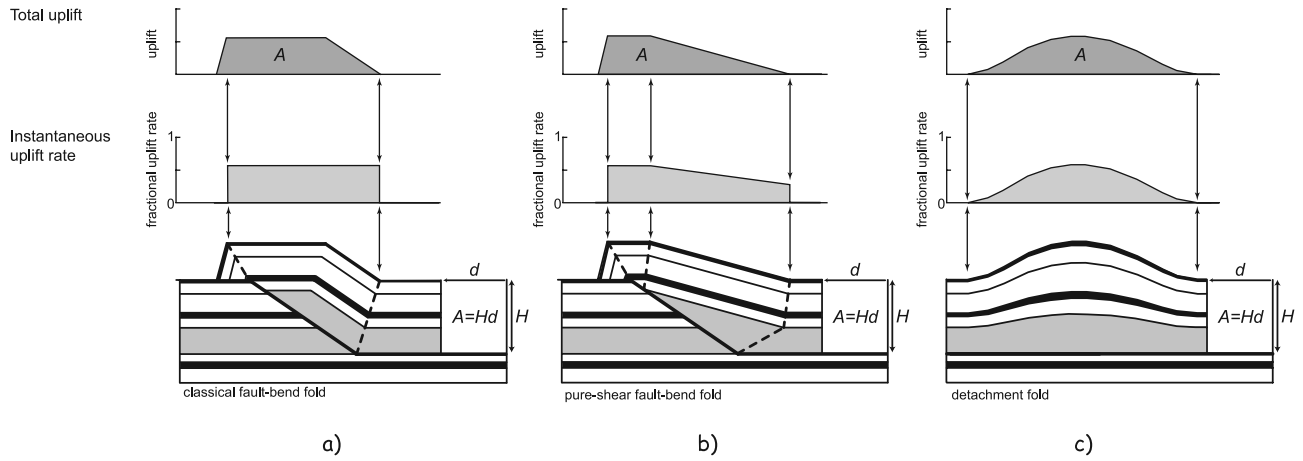

Figure 1. Comparisons between instantaneous and total uplift for three simple fold models with identical shortening: (a) classical fault bend fold, (b) pure shear fault bend fold, and (c) detachment fold. The detachment fold model shown in Figure 1c has an instantaneous uplift rate and a total uplift that are collocated (spatially coincident) and linearly proportional. In contrast, the two fault bend folding models in Figures 1a and 1b show noncollocated instantaneous and total uplift such that the instantaneous uplift is not everywhere proportional to the total uplift. The abrupt discontinuities in uplift rate across active axial surfaces in Figure 1a are normally indicative of kink band migration, whereas a slope to the uplift rate over a substantial horizontal distance in Figures 1b and 1c is indicative of limb rotation. The fault bend fold models are based on the models of *Suppe* [1983] and *Suppe et al.* [2004]; the detachment fold model in Figure 1c is similar to the pure shear model of *Epard and Groshong* [1995].

[4] The simplest fault bend folding model (Figure 1a) displays an instantaneous uplift rate that is simply the fault slip rate times the sine of the underlying fault dip, which has been observed on geomorphic timescales [*Hutrez et al.*, 1999; *Lavé and Avouac*, 2000] and even in the coseismic geodetic displacement of a single large shallow earthquake (Chi-Chi earthquake) [*Yue et al.*, 2005]. The active axial surfaces of fault bend fold models are pinned to fault bends and bound regions of different underlying fault dip. Therefore active axial surfaces represent localized discontinuities in uplift rate (Figure 1a). These abrupt transitions in uplift rate appear at the land surface in the form of fold scarps, which are the instantaneous locus of surface folding [*Suppe et al.*, 1997]. For the simple model of a ramp anticline (Figure 1a) the instantaneous uplift will occur only above a fault ramp in the region bounded by the two active axial surfaces. As large slip accumulates, the finite fold becomes displaced with respect to the instantaneous uplift because particles move progressively through the active fold by kink band migration. The instantaneous and total uplift are thus not collocated (not spatially coincident) and produce different shapes. For even more complex fault bend fold structures involving wedging, imbrication and multiple fault bends (Figure 2), the instantaneous uplift rate is still simply the fault slip rate times the sine of the local underlying fault dip. In this paper we focus considerable attention on the geomorphic and stratigraphic effects of active axial surfaces intersecting the topographic surface in the Quilitak anticline, especially the generation of fold scarps.

[5] In contrast with classical fault bend folding driven by its characteristic kink band migration, many other significant folding mechanisms predict limb rotation or a combination of limb rotation and kink band migration, including detachment folding, trishear fault propagation folding and shear fault bend folding (Figure 1) [*Erslev*, 1991; *Epard and Groshong*, 1995; *Poblet et al.*, 1997; *Hardy and Ford*, 1997; *Allmendinger*, 1998; *Suppe et al.*, 2004]. For example, detachment fold growth can be modeled using a self-similar heterogeneous pure shear model in which the instantaneous uplift rate is a linear function of the finite uplift at any point (Figure 1c) [cf. *Epard and Groshong*, 1995]. During an earthquake or other increment of deformation, surface warping is spread continuously over the entire structure and is not characterized by abrupt transitions in uplift rate, in contrast with fault bend folding. This simple model predicts that a young deformed geomorphic surface would be spatially coincident with the finite fold structure and have the same shape but at a reduced linearly proportional amplitude. Total uplift and instantaneous uplift rate are collocated, in contrast with classical fault bend folding. In this paper we show evidence for such linearly proportional collocated uplift in Yakeng anticline.

2. Tectonic Setting of Active Folding

[6] The Tian Shan range is a locus of active compression induced by the collision between India and Asia [*Molnar and Tapponnier*, 1975; *Tapponnier and Molnar*, 1979]. It is one of the largest and most active intracontinental mountain ranges (Figure 3) [*Avouac et al.*, 1993; *Molnar and Deng*, 1984]. Up to 20 mm/yr of shortening [*Abdrakhmatov et al.*, 1996; *Reigber et al.*, 2001; *Molnar and Ghose*, 2000] is accommodated in thrust belts on both sides and within the range [*Allen et al.*, 1999; *Burchfiel et al.*, 1999; *Burbank et*

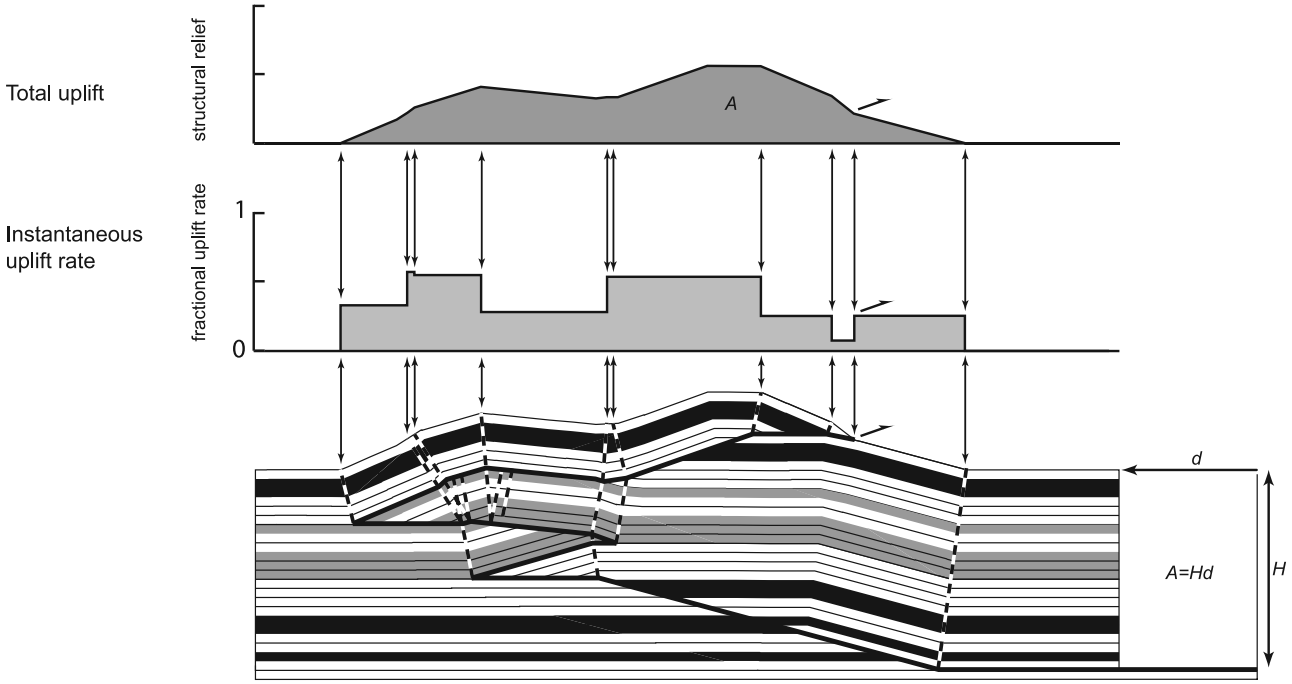

Figure 2. A complex fault bend fold model showing many discontinuities in the instantaneous uplift rate across active axial surfaces, which is indicative of kink band migration. The uplift rate is everywhere equal to the sine of the underlying fault dip times the local fault slip rate. The instantaneous uplift rate and total uplift are neither collocated nor proportional.

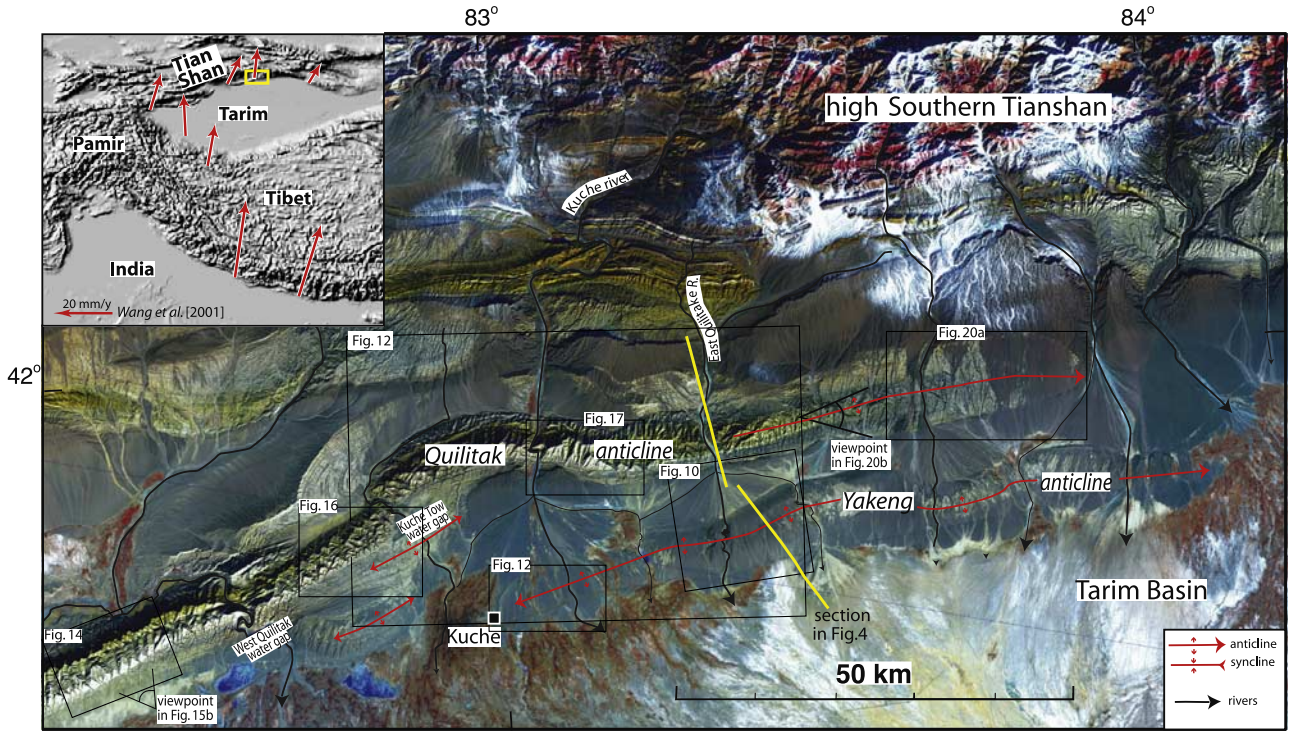

Figure 3. Eastern end of Kuche fold-and-thrust belt, southern Tian Shan. Present deformation is localized almost entirely along the Quilitak and Yakeng anticlines. Boxes are areas of Figures 10a, 12, 14, 16, 17, and 20a. Viewpoints of Figures 15 and 20b and location of the seismic line of Figure 4 are shown. Inset gives location of Tian Shan range within the framework of the Indo-Eurasia collision and GPS data of *Wang et al.* [2001]. Box is area of Figure 3.

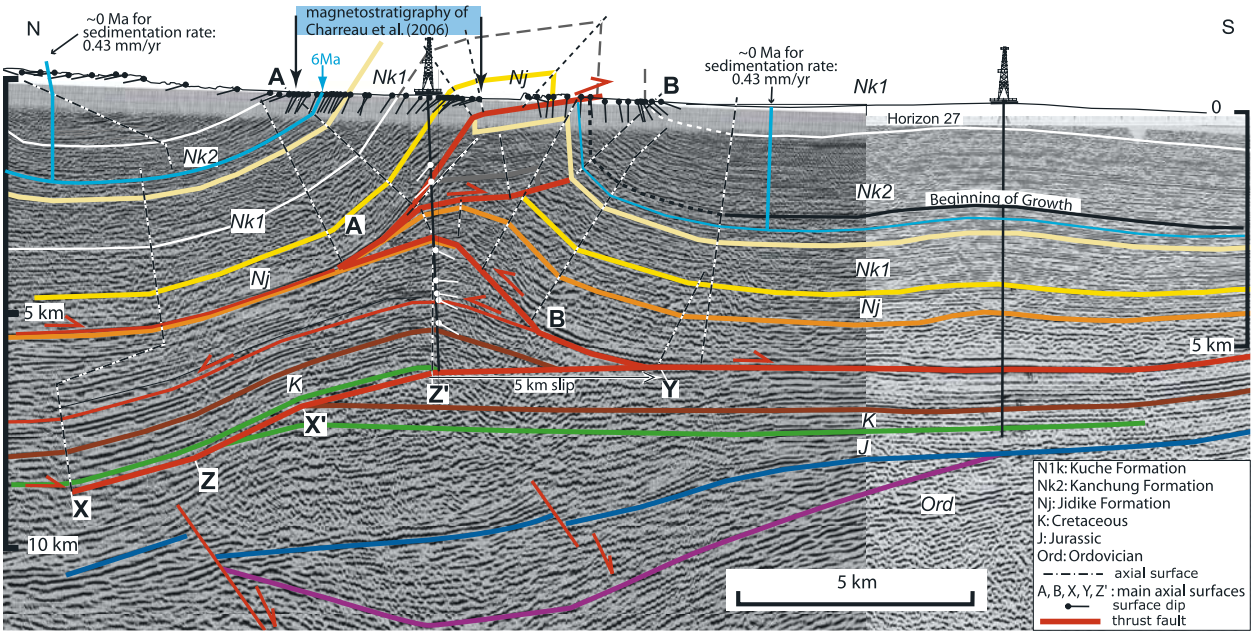

Figure 4. Balanced cross section across the Quilitak and Yakeng anticlines along the East Quilitak River integrating surface geology, seismic reflection profiles, and well data (see Figure 3 for location). Location of 6 Ma time horizon (blue line) in northern Quilitak syncline is from magnetostratigraphy of *Charreau et al.* [2006]. Location of 6 Ma time horizon (blue line) in southern syncline is at the same stratigraphic level as the 6 Ma horizon in the northern syncline. The stratigraphic thickness (vertical blue lines) in both synclines above the 6 Ma time horizon is consistent with a constant 0.43 mm/yr sedimentation rate.

al., 1999; *Chen et al.*, 2002; *Thompson et al.*, 2002; *Hubert-Ferrari et al.*, 2005b]. In the eastern part of the southern Tian Shan between 80°30′ and 85°E, the main locus of deformation is the 350-km-long Kuche fold-and-thrust belt that deforms an 8- to 10-km-thick Triassic to Recent sequence of continental strata [*Yin et al.*, 1998]. In the Kuche belt, active deformation is accommodated mainly on its southern edge by the Quilitak and Yakeng anticlines [*Burchfiel et al.*, 1999] where active faulting is mostly blind, but folding is well expressed at the surface. In addition, seismic reflection profiles and drilling image the deep structures of both anticlines. The relationships between the surface morphological expressions and the related faulting and folding processes at depth can therefore be addressed.

[7] The Yakeng and Quilitak anticlines show strongly contrasting surface morphology. Their dissimilarities reflect differences in underlying fold mechanisms and in total shortening consumed by folding with associated variation in fold amplitude. The Yakeng anticline is barely visible in large-scale satellite images and topographic maps and forms a low ridge that extends for about ~110 km parallel to the Tian Shan with a width of 5–8 km and maximum topographic relief of 150 m (Figure 3). The near-surface internal structure is exposed along a few major transverse valleys that are incised into the ridge and show it to be a gentle anticline with limb dips of 3°–4° in Quaternary dark gray conglomerates and yellow gray sandstones. Seismic lines show that the Yakeng anticline at depth is similar but somewhat broader (~10 km) than its active surface expression, with the flanks being buried by recent sedimentation.

[8] In contrast, the Quilitak anticline is expressed topographically as a rugged and largely inaccessible mountainous ridge that extends for about 225 km along the Tian Shan with a 5–7 km width and maximum relief of ~1 km (Figure 3). Seismic lines show that the Quilitak anticline is substantially wider at depth (10–20 km), where it is characterized by gently dipping flanks (10°–30°) (Figure 4). The low-dipping flanks in many places are buried by recent sediments and elsewhere are exposed as regions of low relief adjacent to the high-relief ridge. The Quilitak ridge exposes a tight anticlinal core of Miocene to Pleistocene strata with steeply dipping fold limbs that are in many places nearly vertical or overturned.

3. Yakeng Anticline: A Classic Detachment Fold

3.1. Deep Structure and Growth Analysis

[9] The contrasting deep structure of the Yakeng and Quilitak anticlines is illustrated in a cross section along the East Quilitak valley (Figure 4, see location in Figure 3). This section integrates surface geology, seismic reflection profiles and well log data. The seismic reflection profiles were depth converted using a velocity model obtained from stacking velocities and calibrated using wells. The velocity model was generated using the procedure of *Süss and Shaw* [2003]. The Yakeng fold is characterized by gentle warping above a detachment level, whereas Quilitak

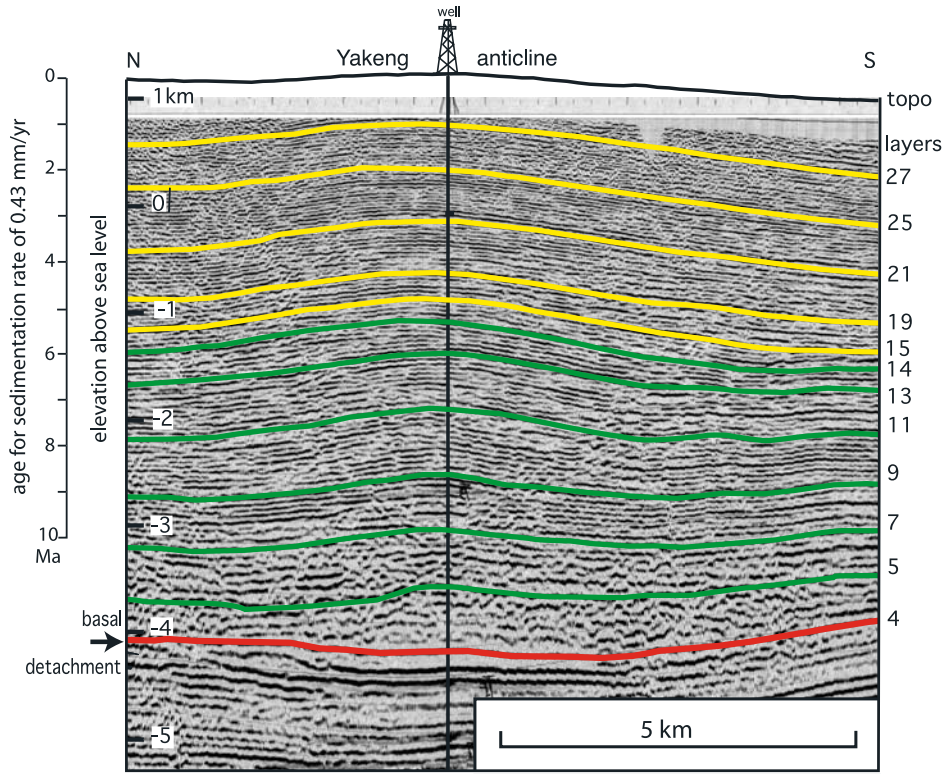

Figure 5. Yakeng detachment fold (see location in Figure 3). Seismic profile shows gentle upward warping of distinctive sedimentary layers above a basal detachment. The 27 seismic horizons mapped through the structure indicate that no topographic emergence occurred until after horizon 27. The timescale on the left is interpolated from a constant sedimentation rate of 0.43 mm/yr from *Charreau et al.* [2006].

is a fault bend fold with a relatively simple deep thrust ramp overlain by a complex wedge system responsible for the steep to vertical dips on both limbs of the anticline at the surface.

[10] The deep structure of Yakeng is similar to its surface expression (Figures 4 and 5). It extends to a depth of 5–6 km as a broad, smoothly curved anticline with limbs that dip generally 5°–6° or less. The amplitude and area of structural relief of the fold progressively decrease downward to a 6 km deep evaporitic basal detachment horizon in the Jidike Formation (horizon 4, Figures 5 and 6a) [*Hubert-Ferrari et al.*, 2005a]. This same detachment horizon is the upper detachment of the deep ramp of Quilitak anticline and thus provides the direct fault link at depth between the Yakeng and Quilitak structures.

[11] We have quantified the magnitude of shortening and history of growth of Yakeng [*Hubert-Ferrari et al.*, 2005a] using a modification of the method of *Epard and Groshong* [1995] based on measurements of area relief in the thickness domain combined with conservation of area [*Gonzalez-Mieres and Suppe*, 2006, also Analysis of growth of detachment folds, submitted to *AAPG Memoir*, 2006, hereinafter referred to as Gonzalez-Mieres and Suppe, submitted manuscript, 2006]. Measurements of area of relief as a function of elevation for 27 mapped horizons of Yakeng yield a well-constrained total shortening of 1200 m based on the rate of change of area of relief with respect to height in the pregrowth interval (horizons 5 to 14) (Figure 6b). A marked inflection in the rate of change of relief indicates the beginning of growth at horizon 15 (Figure 6b). Furthermore there is a significant excess area $A_e \approx 0.83$ km^2 within the core of the fold at the level of the basal evaporitic detachment layer as given by the nonzero intercept of the linear regression at horizon 4 which is the bottom of the detachment layer (see Figure 6b). This excess area may be an effect of minor flow in the basal evaporitic layers into the core of the fold, although other explanations of excess area are possible [*Suppe*, 2006]. The mean shortening $\overline{S}$ between the detachment and any horizon is given by

$$\overline{S} = \frac{A - A_e}{H} \tag{1}$$

where A is the area of structural relief for that horizon, A_e is the excess area and H is the height above the detachment (Figure 7 and Table 1). Equation (1) assumes that flow of the basal layer occurred later as discussed below. The ratio of shortening rate to sedimentation rate $d\overline{S}/dH$ has been nearly constant ($\sim$0.32–0.40) between the beginning of growth and the topographic surface, with $\sim$950 m of shortening and 2.3 km of sedimentation. As discussed below, this ratio has increased by an order of magnitude (to $\sim$3.3)

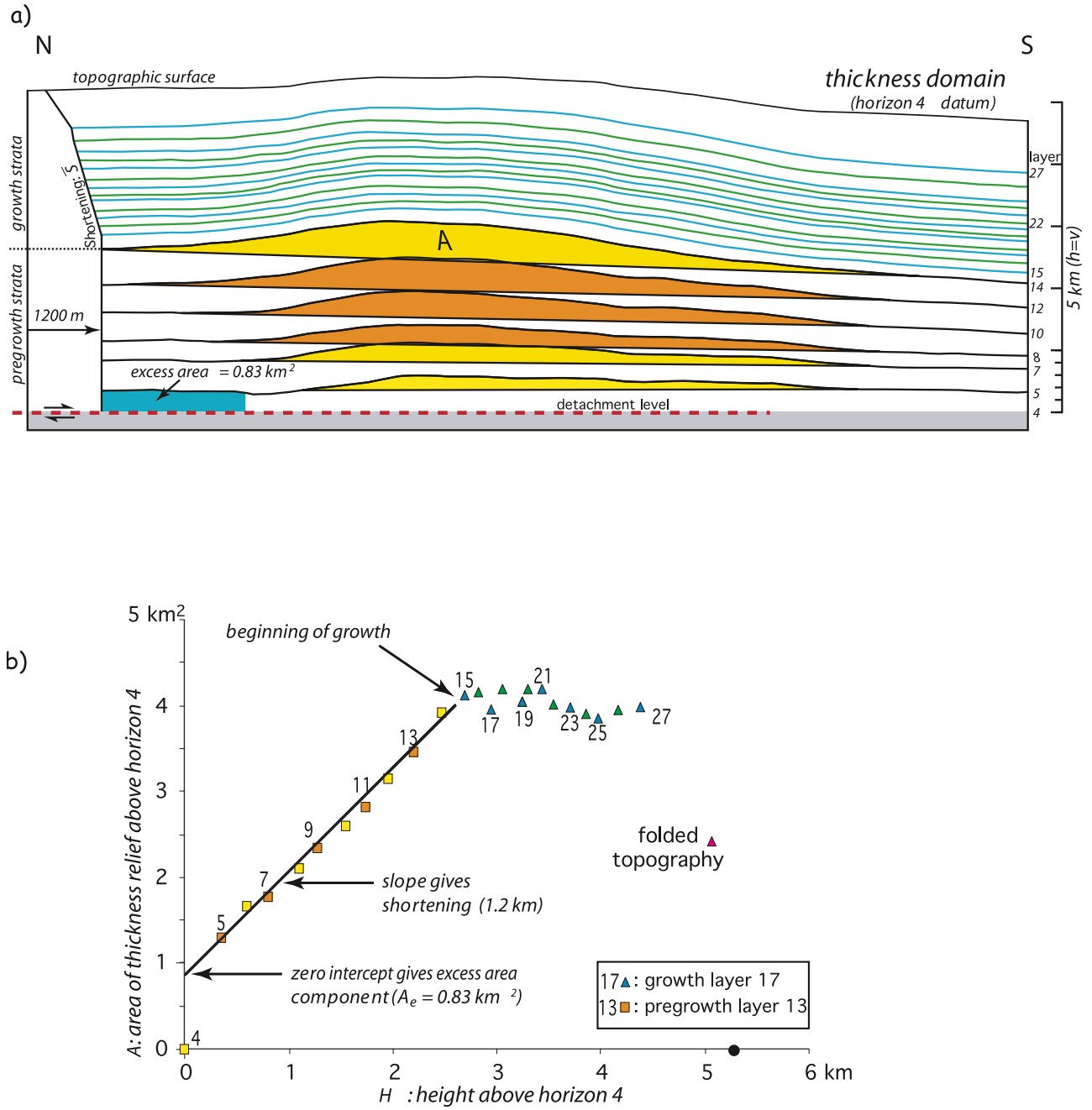

Figure 6. (a) Yakeng anticline flattened to horizon 4 (horizontal scale equal to vertical scale). By this process, stratigraphic gradients are identified and we get a reliable measurement of area of structural relief (A) and undeformed height (H). This analysis shows that horizons 5–14 have undergone 1200 m of shortening and thickening above an evaporitic detachment (see Figure 6b). There is an additional 0.83 km^2 excess area in the basal layer (4–5) [*Hubert-Ferrari et al.*, 2005a]. (b) Area of structural relief as a function of height above detachment horizon 4. The slope of the linear increase in area of relief between layers 5 and 15 indicates a constant shortening of 1200 m. The nonzero intercept indicates an excess area of 0.83 km^2 within the basal evaporite interval (4–5). The beginning of growth is horizon 15 or 16.

since the deposition of the deformed topographic surface, with ~250 m shortening during a period in which ~70–90 m sedimentation occurred in the Tarim basin south of Yakeng. Therefore the deformation rate of Yakeng must have greatly increased recently, whereas sedimentation rate stayed nearly constant because base level changes are regionally controlled in the Tarim basin. Seismic reflector geometry (Figure 5) shows no evidence of any prior topographic emergence exceeding the seismic resolution prior to horizon 27 time.

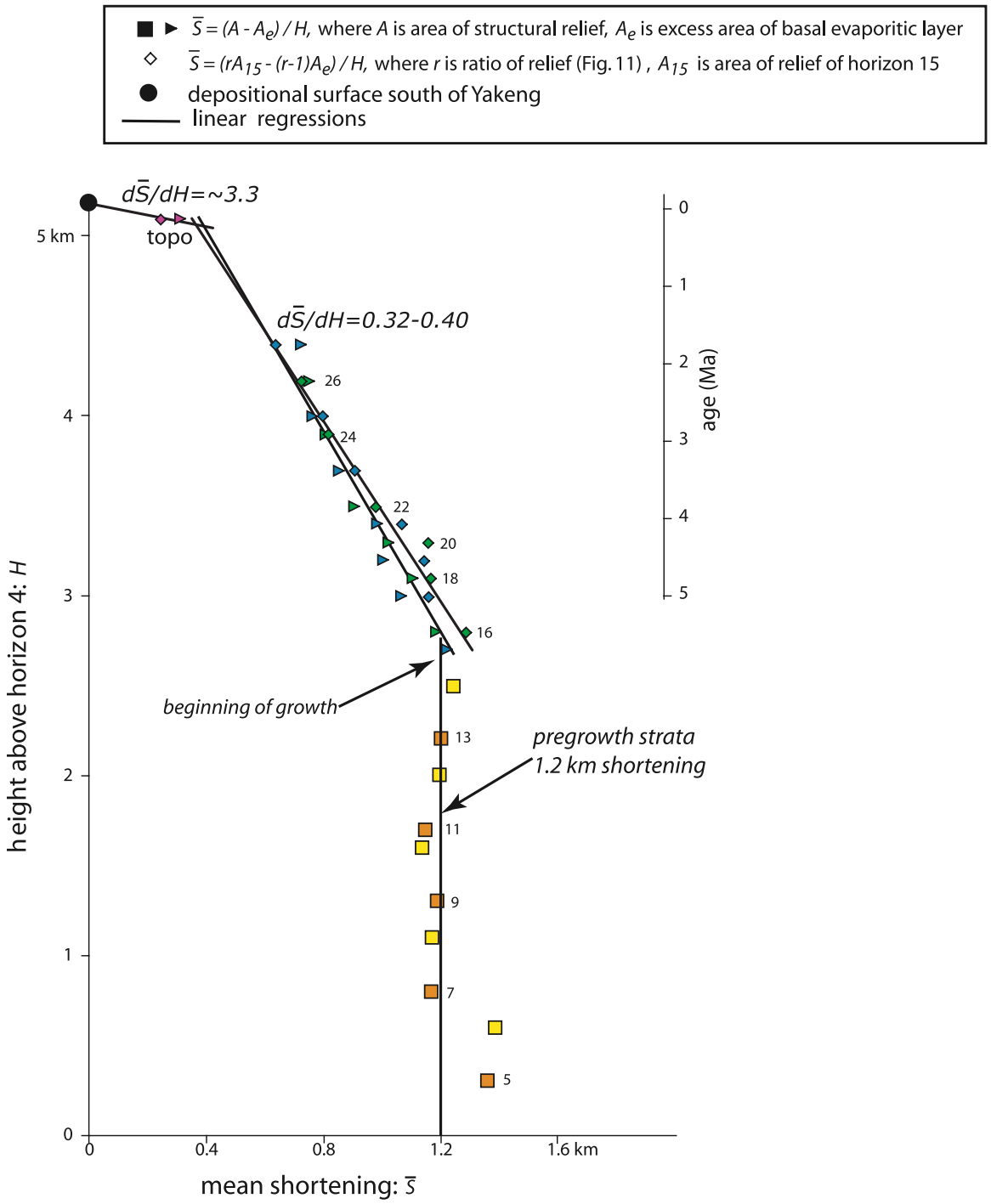

Figure 7. Shortening accommodated in Yakeng anticline. Shortening is calculated from area of relief minus the excess area (squares and triangles) based on equation (1) and from relief regression relative to pregrowth horizon 15 (diamond) as discussed in the text (see equation (4)). Linear shortening within the growth interval (15–27) implies constant sedimentation rate, suggesting a late development of excess area in the basal evaporitic layer (equation (1)) or a growth in excess area coupled to shortening (equation (2)). Larger apparent shortening of layers 5–6 suggests a small additional excess area component [see also *Gonzalez-Mieres and Suppe*, 2006, also submitted manuscript, 2006].

[12] A nearby magnetostratigraphic study across the steep north limb of the Quilitak anticline (along the line of Figure 4) provides excellent age control over a 3000-m-thick section between 13 and 5 Ma [*Charreau et al.*, 2006]. This study shows a remarkably constant sedimentation rate of 0.43 mm/yr over the interval 5–10 Ma. Extrapolation of this rate to the top of the stratigraphic section north of the Quilitak anticline yields an approximate zero age for the top

Table 1. Yakeng Anticline Shortening[a]

Horizon	Height H Above Detachment h4, km	Area of Structural Relief A_s, km^2	Relief Ratio From Regression r	Regression Parameter R^2	Shortening FromArea of Relief $\overline{S}_a$, km	Shortening From Ratio of Relief $\overline{S}_r$	Regional Stratigraphic Gradient
5	0.3	1.30			1.36		
6	0.6	1.66			1.39		
7	0.8	1.77			1.17		
8	1.1	2.11			1.17		
9	1.3	2.34			1.19		
10	1.6	2.60			1.14		
11	1.7	2.82			1.15		
12	2.0	3.15			1.19		
13	2.2	3.46			1.20		
14	2.5	3.92			1.25		
15	2.7	4.12	1	1	1.22	1.22 km	1.15°
16	2.8	4.15	0.8959	0.99	1.18	1.29	1.15°
17	3.0	3.95	0.8702	0.99	1.06	1.16	1.03°
18	3.1	4.20	0.9000	0.99	1.10	1.17	1.00°
19	3.2	4.05	0.9053	0.99	1.00	1.14	0.97°
20	3.3	4.20	0.9395	0.97	1.02	1.16	0.97°
21	3.4	4.19	0.9023	0.98	0.98	1.07	0.97°
22	3.5	4.02	0.8596	0.99	0.90	0.99	1.09°
23	3.7	3.98	0.8447	0.99	0.85	0.91	1.20°
24	3.9	3.91	0.8084	0.99	0.80	0.81	1.26°
25	4.0	3.85	0.8119	0.96	0.76	0.80	1.26°
26	4.2	3.94	0.7800	0.97	0.75	0.72	1.15°
27	4.4	3.98	0.7352	0.98	0.72	0.64	1.15°
topo	<5.1	>2.42	0.4212	0.92	>0.31	0.25	0.58°

[a] $\overline{S}_a = (A_s - A_e)/H$, mean shortening computed from area of structural relief with excess area A_e = 0.83 km^2; $\overline{S}_r = [rA_{15} + (r - 1)A_e]/H$, shortening computed from ratio of relief.

of the section, therefore a nearly constant sedimentation rate of ~0.43 mm/yr between 10 Ma and the present is indicated. This constant sedimentation rate is consistent with the observed constant ratio of shortening rate to sedimentation rate for all the preemergent growth horizons (Figure 7) and with the balanced cross section of Quilitak (Figure 4). The reason that the same sedimentation rate is valid for both north and south of the Quilitak anticline is because the observed regional gradients in the thickness of the growth interval are slight (Figure 4) [see also *Hubert-Ferrari et al.*, 2005a]. In contrast with many foreland basins, the sedimentation rate near Kuche is not dominated by local tectonic effects such as basement flexure or sediment supply, but rather by the regionally steady rise of base level for the entire closed Tarim basin, which is controlled by the integrated effects of a vast region (Figure 3, inset). A similar nearly constant sedimentation rate of 0.31–0.33 mm/yr over the last 5 Myr is indicated ~150 km to the east in wells [*Sun et al.*, 1999]. Adopting this constant sedimentation rate chronology for the Yakeng-Quilitak area predicts a beginning of growth for Yakeng (horizon 15) at ~5.5 Ma (Figures 4 and 5), a topographic emergence at ~0.16–0.21 Ma and shortening rate of ~0.16 mm/yr for Yakeng between horizon 15 and the deformed topographic surface. The average shortening rate since emergence is then ~1.2–1.6 mm/yr.

[13] Some ambiguity exists over the timing of development of the excess fold area A_e in the basal evaporitic layer (Figures 6 and 7), particularly if we consider only the areas of relief as a function of height (Figure 6b), because A_e is a modest fraction (~20%) of total structural relief at horizon 15. The above computation of shortening by equation (1) assumes that evaporitic flow (or other processes responsible for the excess area) occurred entirely after deposition of the growth horizons; this yields a nearly constant rate of shortening relative to sedimentation since ~5.5 Ma until emergence, which is an attractive hypothesis because of the observed constant sedimentation rate. Alternatively, it is possible that this growth in excess area is distributed smoothly through some or all of the growth section, representing a process coupled to the shortening [*Suppe*, 2006], such that some fraction f of the total excess area A_e developed after the deposition of the horizon in question. Equation (1) becomes

$$\overline{S} = \frac{A - fA_e}{H} \tag{2}$$

If, for example, f is a linear function of height for the preemergent growth interval, the mean shortening increases by 10–20% over equation (1). However, *Hubert-Ferrari et al.* [2005a] pointed out that considering the spatial distribution of relief due to A_e, it appears that a substantial fraction of the excess area could be late. The locus of relief of the basal evaporitic layer (horizon 4–5) is displaced ~3 km to the south of the total relief due to shortening (horizons 5–15), but is collocated with the relief postdating horizon 27 (topo-27) (Figure 8). The distribution of relief postdating horizon 27 (topo-27) thus appears to include a significant fraction of A_e whereas the older growth sequence (horizon 15–27) may not. Therefore late flow of evaporites into the core of the fold may have contributed to topographic emergence; however, the order-of-magnitude increase in the rate of shortening associated with emergence is required by the relief data regardless of the timing of the basal flow [see

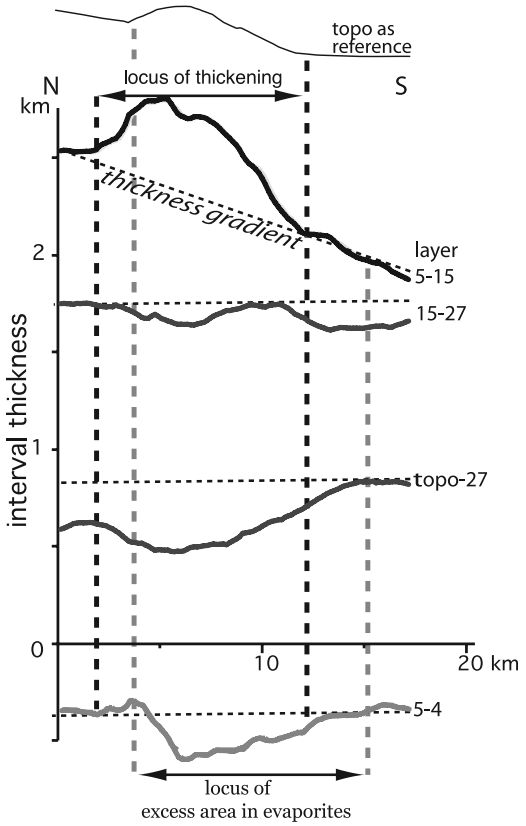

Figure 8. Present thickness variations across Yakeng anticline, which helps separate structural and stratigraphic components of the fold shape. The basal evaporitic interval (4–5) shows thickness variation presumably caused by flow. Interval 5–15 shows regional northward stratigraphic thickening reflecting syndepositional flexure of the basement, plus local structural thickening at Yakeng. The overlying interval 15–27 shows stratigraphic thinning over Yakeng indicating growth. The uppermost interval (topo-27) shows thinning over Yakeng, indicating accelerated growth including the development of excess area throughflow of the basal layer [*Hubert-Ferrari et al.*, 2005a].

also *Gonzalez-Mieres and Suppe*, 2006, also submitted manuscript, 2006].

3.2. Morphological Expression of an Emergent Detachment Fold

[14] At the surface Yakeng forms a low asymmetric ridge (Figures 3, 5, and 9) characterized by a 1.3-km-wide nearly flat top, a 1.7-km-wide back limb and a much wider 5-km-long front limb (Figure 10). Even though its topographic relief is modest, the emergence of this ridge has strongly disrupted the river networks by changing topographic gradients (Figures 9 and 10). The river responses have depended mainly on stream power [e.g., *Howard and Kerby*, 1983; *Howard et al.*, 1994; *Burbank et al.*, 1996a, 1996b]. Rivers with relatively high stream power have been able to maintain their original courses by incision (Figure 10). Some rivers have adopted a southward converging pattern along the Yakeng northern limb, which increases their stream power sufficiently to continue incising. Rivers with relatively low stream power have been diverted and flow along the base of the Yakeng northern limb parallel to the fold axis [e.g., *Burbank et al.*, 1999; *Humphrey and Konrad*, 2000]. Finally, a new northward flowing drainage system was established along the Yakeng northern limb.

[15] The rise of Yakeng above the river base level has also locally lowered river gradients producing increased local sedimentation upstream and downstream of the fold [*Ouchi*, 1985; *Holbrook and Schumm*, 1999]. Upstream of Yakeng five major rivers crossing the high Quilitak ridge have deposited the bulk of their bed load producing dark gray pebble conglomerate in alluvial fans (Figure 9). The amount of sediment deposited and the size of related alluvial fans depend mainly on the river size or stream power [e.g., *Humphrey and Konrad*, 2000]. The biggest fan is that of the Kuche River, which entirely covers the western plunging nose of the Yakeng anticline. The other fans have a more restricted extension, and fill the 5- to 10-km-wide low area in between the Quilitak ridge and the emergent Yakeng ridge. Downstream of Yakeng sedimentation includes the development of small dark gray alluvial fans that cover part of the south limb of Yakeng. Farther south the sedimentation pattern changes, and yellow to gray sandstones and siltstones, which are typical Tarim basin sediments, have been deposited on the far southern limb of Yakeng.

[16] Active sedimentation has partly modified the surface expression of the fold relative to its deep structure. The surface width of Yakeng (8 km in Figure 10) is, in fact, narrower than the 13-km-wide deep fold structure (Figure 5) because of continuous burial of the anticlinal flanks (Figure 11). The surface expression thus does not fully reflect the area over which active uplift occurs, but represents a trade-off between surface and tectonic processes. Yakeng emergence occurs only where uplift rate is greater than sedimentation rate. Some variation in the morphological expression of the Yakeng anticline along strike may be accordingly interpreted as dominated by sedimentation processes, and not by structural change along strike. For example, the northern edge of the emergent Yakeng high has a sinuous contact in map view, which strongly contrasts with its straight southern edge (Figure 9). The north edge of the emergent Yakeng is closer to Quilitak away from the apex of all the major fans deposited in between the two anticlines. This phenomenon may simply reflect variation in sedimentation rate, which is higher at the fan apexes than at their edges. A locally higher sedimentation rate would imply a local higher capacity to bury Yakeng and balance its uplift rate. The latter pattern is possible only if uplift rate varies smoothly across the Yakeng structure.

3.3. Linearly Proportional Growth of the Yakeng Detachment Fold

[17] Up to this point we have only used areas of relief and mass balance considerations to constrain the shortening and growth history of the Yakeng anticline (Figures 6 and 7). We have not yet made any use of information on

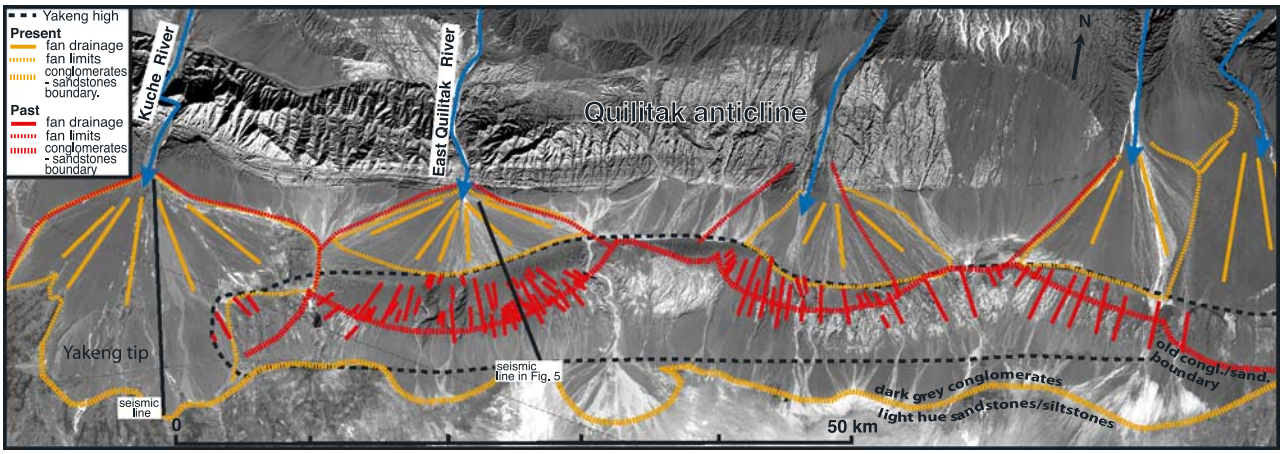

Figure 9. Inherited preemergence fan morphology preserved in the Yakeng detachment fold. The present Yakeng topographic ridge, though subtle, disrupts river networks and enhances sedimentation upstream and downstream. The major facies change between dark conglomerate and light sandstone deposition occurs today south of Yakeng. The morphology prior to topographic emergence was completely different: the large alluvial fans emerging from the water gaps of Quilitak anticline extended farther south than today. The southern edges of these preemergent fans are recorded by the conglomerate-to-sandstone facies change, which lie within the emergent Yakeng anticline and 5–10 km north of its present location. Former fan drainages are still preserved on the anticlinal crest and have channel orientations shown as black lines that project to the present fan apices at the edge of Quilitak (see also Figure 10b).

fold shape. We can more fully constrain both the folding kinematics and history by comparing the shape of the emergent Yakeng surface with the shapes of the directly underlying seismically imaged horizons. We use the topographic profile and profiles of the underlying growth horizons to measure their relief as a function of horizontal position relative to pregrowth horizon 15 (Figure 11a). Remarkably, these measurements yield a strong linearly proportional relationship both in relief and elevation (Figures 11b and 11c). This means that the local relief of the warped topographic surface, as well as the other growth horizons, is pointwise linearly proportional to the finite structure but at a reduced amplitude. Thus, if at a horizontal location x the relief of a reference horizon is $h_o(x)$, then the relief $h(x)$ of some other horizon is observed for all x to be

$$h(x) \approx r h_o(x) \tag{3}$$

For example, the local relief of the emergent topographic surface is 42% of the relief of the uppermost pregrowth horizon (15) and 57% of the relief of the uppermost seismic horizon (27) (Table 1 and Figure 11b). Such linearly proportional ratios of relief are shown for all the growth horizons with very good statistical fits ($R^2 > 0.9$) and an upward decrease in the ratios of relief r (Table 1). This behavior of Yakeng is similar to behavior of the kinematic detachment fold model in Figure 1 that assumed the present uplift rate is a collocated linear function of the finite fold shape at any point.

[18] However, Yakeng differs slightly from this model (Figure 1) because of (1) the existence of primary stratigraphic thickness gradients that contribute to the ratios of relief and (2) the contribution of the growth of excess area to the growth in total relief. If there is a nonzero gradient in primary stratigraphic thickness between two horizons, then their ratio of elevation (Figure 11c), as opposed to

Figure 10. Yakeng morphology in the East Quilitak area. (a) Yakeng forms a 6-km-wide rounded topographic ridge that few rivers can incise, as shown by many wind gaps (left, Spot image; right, morphological interpretation; see location in Figure 3). Northward tilting of the north flank of Yakeng and alluvial deposition both decrease stream gradients, which favors development of a new river network along the northern limb of Yakeng. When Yakeng developed its present topographic expression, part of the former river network was preserved on its crest (see also Figure 10b). The latter is in straight continuity with present East Quilitak fan network (thick dashed lines Figure 10a), attesting that the fan extended across Yakeng. The old southern edge of East Quilitak fan was located ~4 km southward as shown by the facies boundary between dark fan conglomerates and light Tarim sandstones (see also Figure 9). Box is area of Figure 10b. (b) Present river network formed by a combination of old fan drainage preserved on anticlinal crest and newly established drainage along Yakeng steepest flanks. Former river geometry yields southward converging drainage networks interrupted by wind gaps at Yakeng crest.

relief (Figure 11b), will include this stratigraphic gradient in addition to the structural relief. Therefore the stratigraphic gradients must be removed if we want to quantify the deformational component, particularly for determining the shortening from the ratios of relief. The effect of these stratigraphic gradients on the ratio of relief is small but not entirely negligible in the case of Yakeng (<4%), so we have removed them in determining the ratios of

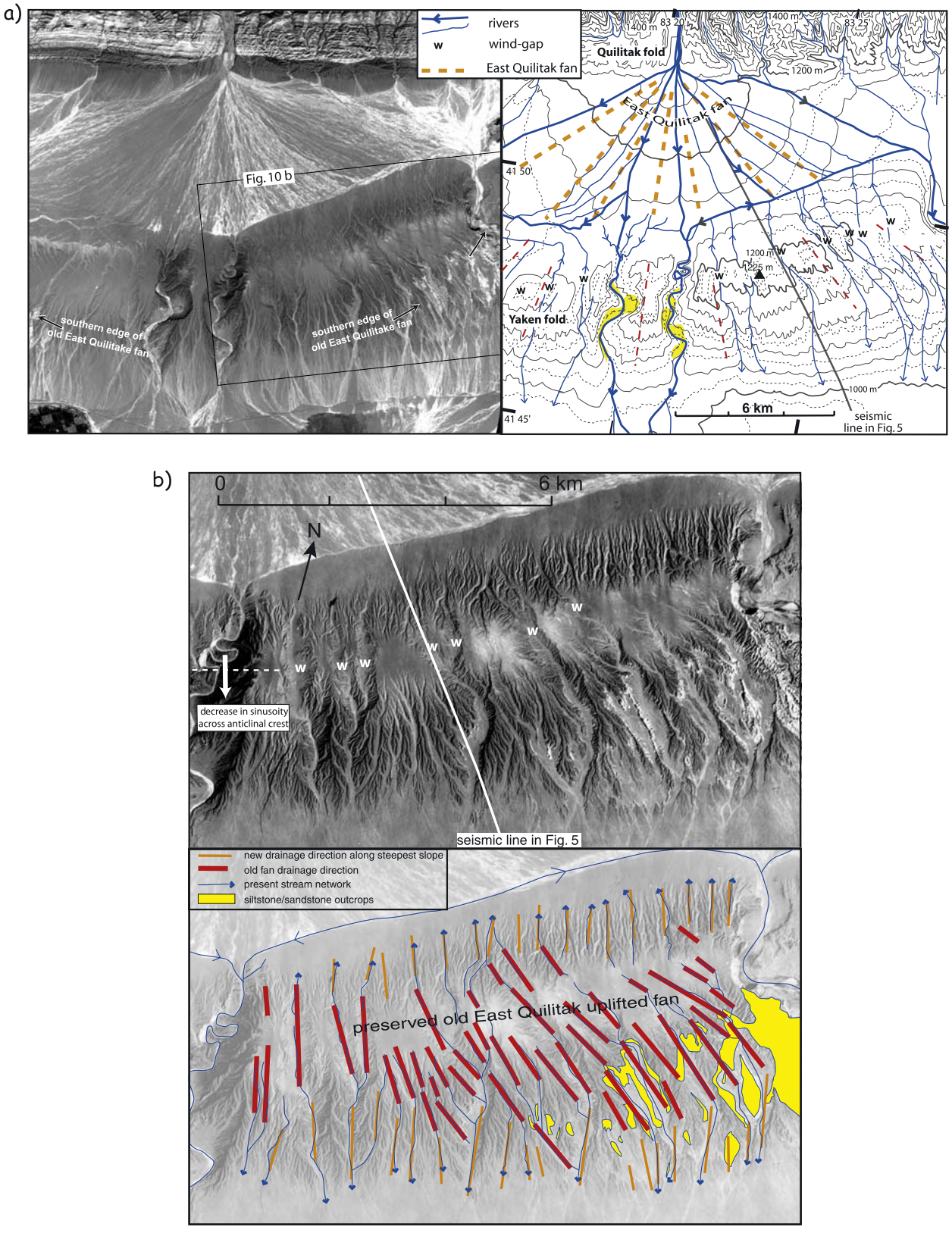

Figure 10

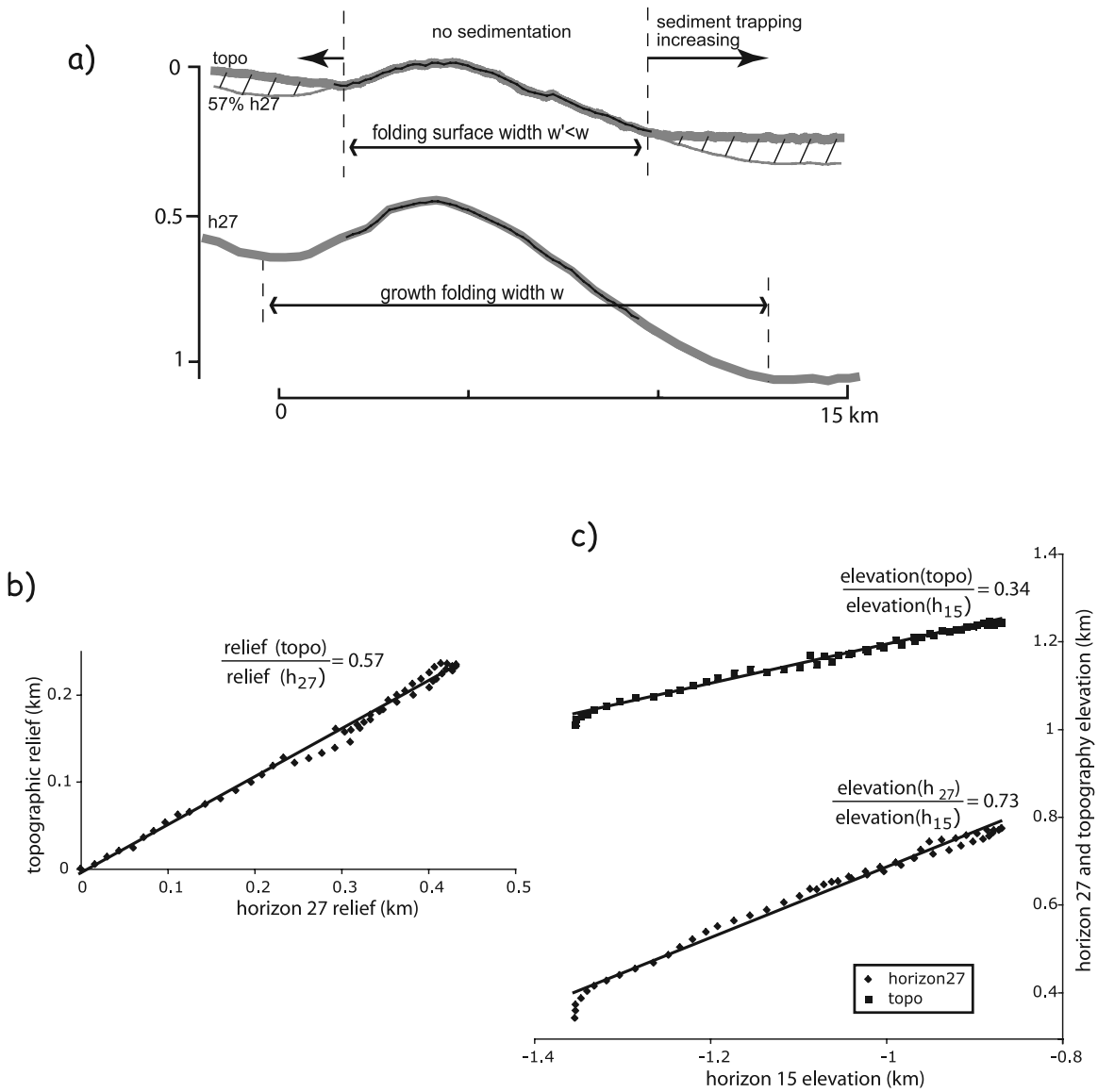

Figure 11. Linearly proportional collocated growth of Yakeng. (a) Digitized shapes of the topographic surface and the underlying growth horizon 27 (see Figure 5). The folded topographic surface that has emerged on the crest of the anticline is buried on its flanks. We estimate its buried position based on the observed point-wise linear proportionality of elevations and relief (Figures 11b and 11c and Table 1). The folded topographic surface has 55% of the topographic amplitude and 57% of the structural relief of horizon 27, which indicates ~70–90 m deposition south of Yakeng since emergence. This thickness suggests a time since emergence is 160–210 ka based on a long-term sedimentation rate of 0.43 mm/yr. (b and c) Graphs showing the point-wise linear proportionality between fold amplitude on different horizons at the same horizontal position, shown as both relief and elevation. The fold shapes on younger horizons are the same as older horizons but at reduced amplitude, with the fractional amplitude given by the slope of the regression. For example, the present structural relief (elevation minus regional stratigraphic gradient) of the deformed topographic surface is 55% of horizon 27. The relief in elevation of the deformed topographic surface is 45% of the relief of pregrowth horizon 15 relief, and the relief in elevation of growth horizon 27 is 81% of pregrowth horizon 15. All growth horizons show similar point-wise linearly proportional amplitudes (Table 1), similar to the simple detachment fold model of Figure 1c. This linear relationship is used to compute shortening in Figure 7 (diamonds).

relief in Table 1. The measured stratigraphic gradients are $1.05 \pm 0.17^\circ$ with adjacent horizons having nearly identical gradients, which yields generally second-order contributions to the ratios of topographic relief because the fold limbs have dips of 4°–7° that dominate the ratios of relief.

[19] The excess area A_e makes a more important and systematic contribution to the ratios of relief. We begin by

noting that it follows from equation (3) that the ratio of relief r between a horizon and a reference horizon such as the uppermost pregrowth horizon (15) is equal to the ratios of their total areas of relief

$$r = \frac{A}{A_{15}} = \frac{\int_o^n r h_{15}(x)dx}{\int_o^n h_{15}(x)dx} \quad (4)$$

and from equation (2)

$$r = \frac{A}{A_{15}} = \frac{\overline{S}H + fA_e}{\overline{S}_{15}H_{15} + A_e} \quad (5)$$

where $\overline{S}H$ and $\overline{S}_{15}H_{15}$ are the contributions of shortening to the total area of relief and f is the fractional contribution of the excess area A_e. Rearranging we obtain the mean shortening between the detachment and the horizon in question

$$\overline{S} = \frac{r\overline{S}_{15}H_{15} + (r-f)A_e}{H} \quad (6)$$

[20] In the case of Yakeng we can approximate the fraction as $f = 1$ given the evidence for significant postemergent excess area (see discussion equations (1) and (2)). Application of this equation to the Yakeng data yields shortening within the growth interval based on regressions of relief that are generally within a few percent of shortening obtained from area of structural relief (Figure 7 and Table 1).

[21] Using this linear growth model, we can estimate the magnitude of sedimentation on the flanks of Yakeng during its latest phase of growth and emergence (Figure 11a). We use the proportional relationship between the elevations of the deformed topography and horizon 27 (Figure 11b) to compute the subsurface shape of the time horizon representing the present emergent topographic surface by taking an unburied topography that is 55% of horizon 27 (Figure 11a). In this way we infer that about 70 to 90 m of sediments were deposited on the edges of the anticline. Given the long-term sedimentation rate of ~0.43 mm/yr controlled by base level, we infer an emergence of the Yakeng anticline at ~160–210 ka. This age of emergence may not coincide precisely with the time of acceleration of growth because (1) some acceleration may be needed before the entire surface emerges and (2) the development of excess area may contribute to emergence. The acceleration could begin as much as 60–70 kyr before emergence based on linear extrapolation (Figure 7). The date of emergence combined with a shortening of ~250 m since emergence (Table 1) yields a postemergence shortening rate in the range 1.2–1.6 mm/yr, which is an order of magnitude greater than the preemergent rate of ~0.16 mm/yr. The ratio of sedimentation rate to shortening rate $d\overline{S}/dH$ is 0.32–0.40 preemergence and ~3.3 postemergence (Figure 7).

[22] The flexural contribution to the shortening (the bed length shortening, $S_c = L - L_o$) is about 5% throughout the growth and pregrowth intervals [*Gonzalez-Mieres and Suppe*, 2006, also submitted manuscript, 2006]. Therefore Yakeng is dominated by layer-parallel pure shear and is closely approximated by a linearly proportional collocated growth model (Figure 1). In addition, *Gonzalez-Mieres and Suppe* [2006] have shown that there is no layer-parallel simple shear within the pregrowth section (constant shortening as a function of height).

3.4. Morphological and Stratigraphic Evidence for the Preemergent Yakeng

[23] We make use of the fact that Yakeng was completely buried to further analyze the details of its present morphology. Former complete burial of Yakeng implies that the five large alluvial fans now deformed by the fold did not exist in their present constrained form, where they onlap the north dipping side of the topographic high. Also the rivers emerging from Quilitak were the only source of conglomerates, whereas today Yakeng is also a local source. Therefore the sedimentation processes and associated river networks changed when Yakeng emerged. Part of this morphological change is recorded in the uplifted morphology and stratigraphy of Yakeng.

[24] The present-day location of the conglomerate-to-sandstone facies change is clearly visible 3–5 km south of Yakeng in remote sensing images because the finer-grained Tarim basin sandstones have a much lighter hue than the coarser dark gray conglomerates of the alluvial fans (Figure 9). The preemergence transition between conglomerates and sandstones is exposed 10–15 km north of the present one within the Yakeng uplift (Figure 9). Its shape is arcuate with the center of curvature of each arc being the apex of one of the major fans emerging from Quilitak. Therefore the old sandstone-to-conglomerate transition maps the southern edge of the fan systems as it existed just before topographic emergence of Yakeng.

[25] The orientations of relict river channels preserved on the crest of the Yakeng uplift also radiate from the apices of the major Quilitak fans, confirming the location and extent of the preemergent fans (Figure 9). The old fan shape and the associated river network are particularly well preserved in the East Quilitak area (Figure 10). Characteristic wind gaps with southward converging channels are ubiquitous over the crest of Yakeng attesting to the presence of the previously throughgoing drainage system (Figure 10a). These former drainages can be most clearly mapped on the nearly flat crest of the anticline, forming a radiating pattern of incised channels typical of alluvial fans. These are continuous with the present East Quilitak fan and its apex (Figure 10b). The emergence of Yakeng above the river base level has thus clearly preserved the former fan morphology on its anticlinal crest. The old drainage network is poorly preserved on the limbs of the fold where younger incised channel networks have developed in response to folding of the previous fan surfaces (Figure 10b).

4. Quilitak Anticline: A Complex Fault Bend Fold

4.1. Deep Structure

[26] The 350-km-long Quilitak anticline shows substantial along-strike variation in its geometry [*Guan*, 2004], but it is everywhere composed of two distinct structural levels. As seen in cross section these include (1) a deep thrust ramp that produces a broad deep anticline with limb dips of 15°–

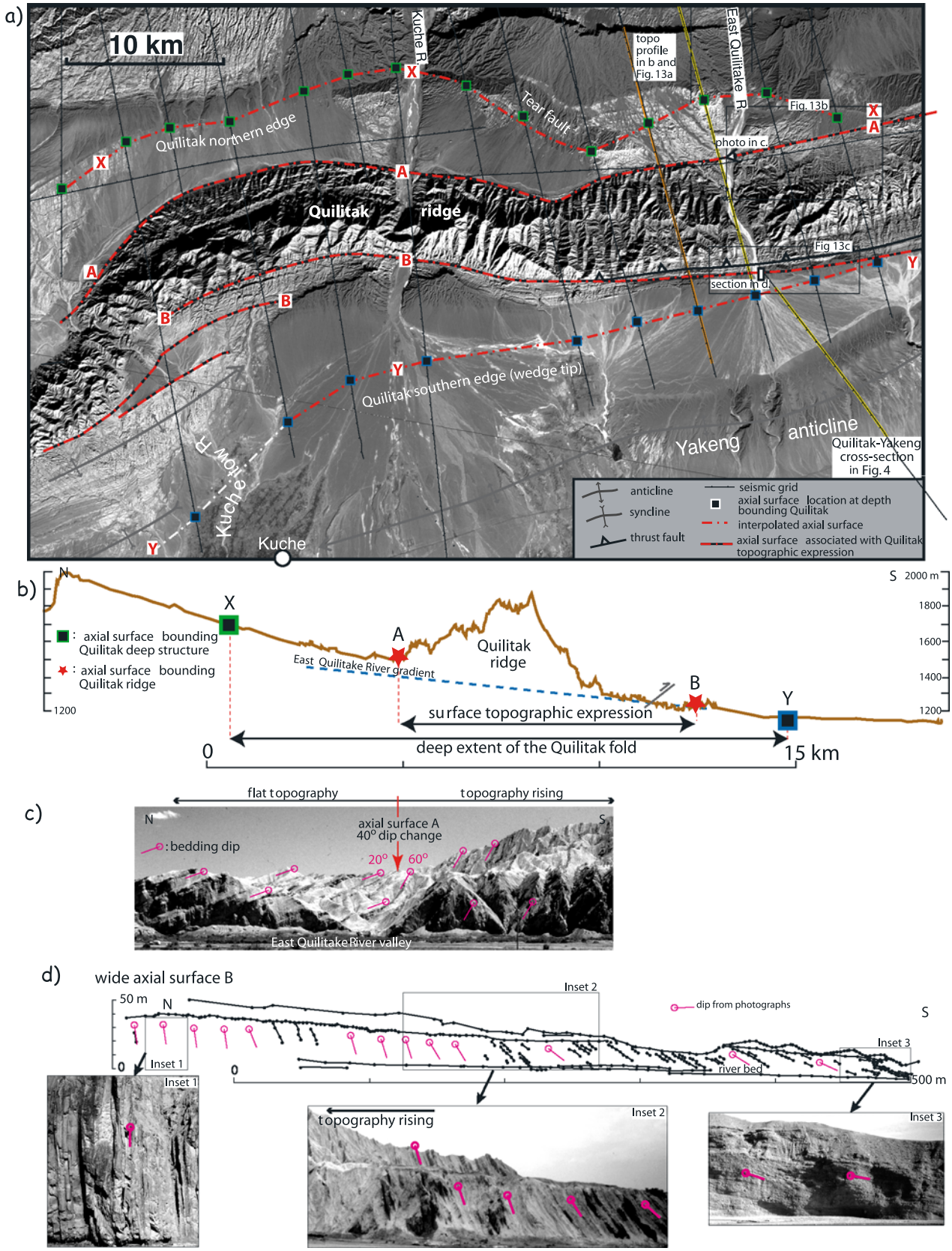
a)
10 km
Kuche R.
East Quilitake R.
topo profile in b and Fig. 13a
Tear fault
Fig. 13b
photo in c.
Quilitak northern edge
Quilitak ridge
Fig 13c
section in d.
Quilitak southern edge (wedge tip)
Yakeng anticline
Quilitak-Yakeng cross-section in Fig. 4
Kuche
Kuche R.
anticline
syncline
thrust fault
seismic grid
axial surface location at depth bounding Quilitak
interpolated axial surface
axial surface associated with Quilitak topographic expression
b)
N
S
2000 m
1800
1600
1400
1200
: axial surface bounding Quilitak deep structure
: axial surface bounding Quilitak ridge
East Quilitake River gradient
Quilitak ridge
surface topographic expression
deep extent of the Quilitak fold
0
15 km
c)
flat topography
topography rising
axial surface A
40° dip change
: bedding dip
20°
60°
East Quilitake River valley
d)
wide axial surface B
50 m
N
S
Inset 1
Inset 2
Inset 3
dip from photographs
river bed
500 m
topography rising

Figure 12

20° and (2) an overlying wedging system that produces the near-vertical dips in its core. Figure 4 shows these two structural levels. A deep thrust ramp steps up southward from a 9-km-deep lower detachment in Upper Jurassic coal horizons to a 5-km-deep upper detachment in evaporates of the Miocene Jidike Formation, which extends southward to form the detachment of the Yakeng anticline. Slip on the deep ramp (6 km), plus deeper folding of the fault, has generated a 7- to 8-km-wide north dipping kink band X-Z' imaged in the seismic profile. This kink band is the convolution of kink band X-X' bounding the footwall fold and Z-Z' bounding the conventional thrust ramp (Figure 4). The deep kink X-X' band is related to a basement fold. Another well-imaged axial surface Y defines the southern limit of the south limb of Quilitak and indicates that 5 km of slip has emerged southward on the Jidike detachment.

[27] However, the shallower structure is necessarily more complex because Yakeng, which is located above the same Jidike detachment, has consumed only 1.2 km of the 5 km slip coming from Quilitak. Much of the remaining 3.8 km is apparently wedged back in the anticlinal core of Quilitak. This wedge geometry implies that the southern axial surface Y, which is pinned to the wedge tip, has functioned as an active axial surface. Above the deep ramp, additional wedging occurs at a shallower level in the anticlinal core. The latter wedge is located at the intersection between the backthrust and an upper bedding-parallel detachment level. At this shallower wedge tip (labeled A in Figure 4) the thrust system splits into two main faults. The upper thrust reaches the surface in the south limb of Quilitak. Slip on the lower thrust is consumed in folding. Additional deep detachment folding and associated wedging in the north syncline completes the slip budget of Quilitak. This back-and-forth wedging system generates a complex set of active axial surfaces interacting with one another in way qualitatively similar to the model in Figure 2.

[28] The first-order along-strike changes in the structure of the Quilitak anticline in the Kuche area can be seen by mapping the most important fault bends and associated axial surfaces at depth, based on a grid of seismic reflection profiles using axial surface mapping techniques [*Shaw et al.*, 1994; *Shaw and Suppe*, 1994]. We mapped the terminations of axial surfaces X and Y, which define the deep extent of Quilitak, corresponding to the base of the deep northern kink band and the southern wedge tip. The resulting axial surface map (Figure 12) shows that the deep extent of the Quilitak anticline narrows substantially from west to east within the Kuche area, changing from 19–25 km west of the Kuche River to 10–12 km east of the East Quilitak River. Approximately half of this eastward narrowing occurs within the southern deep flank of Quilitak that reflects a reduction of fault slip on the deep ramp from 9–10 to 5 km. This eastward reduction in width and slip also is reflected in the eastward plunging topographic relief of the Quilitak core. Ultimately, 70 km east of the Kuche River, the anticline does not show any topographic relief and is covered by a discontinuous unconformable veneer of alluvial sediments (Figure 3).

[29] We note two additional structural changes along strike (Figure 12). First the axial surface X is shifted southward east of the Kuche River without any marked change for the axial surface Y, which reflects a deeper level of the northern base of the deep ramp. Secondly, near the Kuche Tow water gap, axial surfaces X and Y are both shifted southward related to an offset of the entire anticline structure along a major transverse zone near Kuche Tow, which also marks the western limit of Yakeng anticline (Figure 3).

4.2. Large-Scale Morphological Expression of a Fault Bend Fold

[30] The link between the deep structure of Quilitak and its surface morphology is not as simple as for Yakeng. Nevertheless, high-relief topography coincides with the anticlinal structural core characterized by steeply dipping beds. This suggests that a direct relation exists between high topography in Quilitak and the underlying anticlinal structure, as confirmed below.

[31] High relief in Quilitak is characterized by very well defined edges along which a sharp rise in topography occurs. These form continuous linear range fronts labeled A and B (Figures 12a and 12b). These range fronts generally correspond to structural changes and not differences in erodability of uplifted strata. For example, fieldwork conducted along the East Quilitak valley shows that fronts along lines A and B coincide with synclinal axial surfaces along which major (40°–70°) changes in the dip of bedding occur (Figures 12c and 12d). The seismic line located along the East Quilitak River (Figure 4) further confirms that range fronts A and B correspond to intersections between topography and active axial surfaces related to the deep Quilitak wedging system. The Quilitak moun-

Figure 12. Quilitak anticline: relationship between morphology and structure. (a) Axial surface map on top of Landsat image (see location on Figure 3). Black squares indicate the deep locations of footwall terminations of the active axial surfaces X and Y, which indicate the full width of Quilitak anticline at depth (see Figure 4). These terminations can be unambiguously located on seismic lines to within ±100 m except in the tear zone area; the positions of all seismic profiles used are indicated with thin lines. The topographically expressed Quilitak anticline is much narrower than its subsurface extent; the Quilitak high mountainous ridge is bounded by its sharp linear edges A and B, which correspond to active axial surfaces bounding a central region of higher uplift rate, as discussed in text. Box shows the area of Figures 13b and 13c. The locations of the profile used in Figures 12b and 13a, the viewpoint in Figure 12c, and the location of section in Figure 12d are shown. (b) Topographic profile highlights again that the topographic expression of Quilitak is much narrower than the full width of the anticline at depth indicated by axial surface terminations X and Y, which have no topographic expressions. (c) View of 40° dip change along axial surface A. (d) Section logged along eastern edge of East Quilitake River Valley across the wide axial surface B and related field photographs. In Figures 12c and 12d, structural data along the East Quilitak River show that the Quilitak topographic edges A and B correspond to marked change in bedding dip or axial surfaces. The Quilitak topographic high is related to the steep anticlinal core where wedging occurs (see cross section in Figure 4).

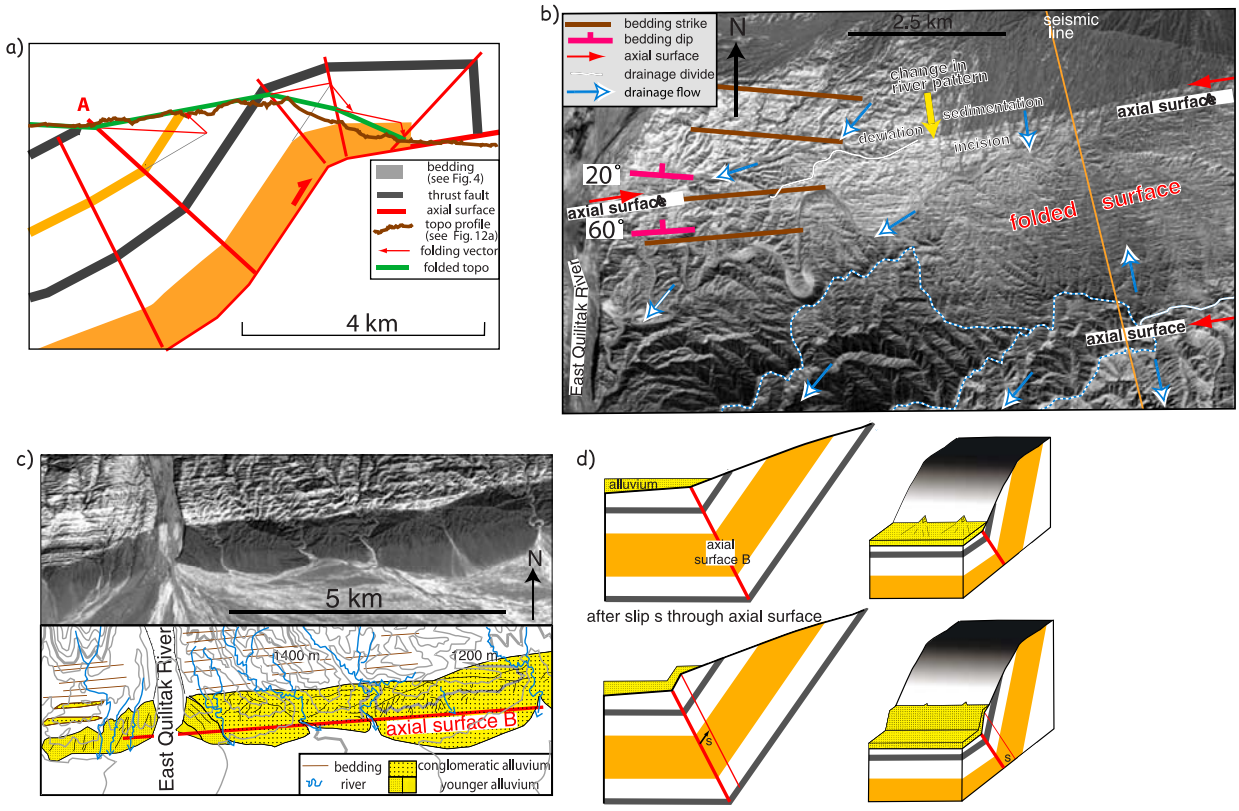

Figure 13. Active folding of the landscape across axial surfaces A and B. (a) Topographic profile (location in Figure 12a) that has a shape similar to that predicted by folding due to slip on the underlying thrust fault. (b) Satellite image showing folding across the same axial surfaces at the surface (location in Figure 12a). Location of seismic lines, which image the deep fold and confirm the interpretation, is marked. (c) Folding of conglomeratic alluvial sediments at the southern front of Quilitak high (location in Figure 12a). (d) Simple fault bend fold model with onlap of recent alluvium over an active axial surface, predicting a morphology similar to Figure 13c.

tainous relief is thus bounded by active axial surfaces, which represent bends on underlying thrust surfaces.

[32] Axial surfaces A and B are active, implying that they mark discontinuities in uplift rate and are the active locus of bending (Figure 1a). The ridge morphology of Quilitak indeed testifies that active folding occurs across both axial surfaces. Figure 13a shows that the predicted shape of the topographic surface due to slip on the underlying thrust through axial surface A, computed using folding vectors [*Shaw et al.*, 2005], is very similar in form and slightly above the observed topographic profile. Therefore the topographic profile is consistent with fault bend folding of the land surface with only modest erosion. Folding of the landscape across the same axial surface just east of the East Quilitak valley is clearly visible in remote sensing images (Figure 13b). In addition, just south of Quilitak ridge,

Figure 14. Southern edge of Quilitak topographic high: West Quilitak area (location in Figure 3). Large triangular fold scarp facets (Figure 15) above a synclinal axial surface mark this southern topographic front. The surface of the triangular facets is interpreted to be the folded equivalent of the low-relief erosional surface that exists south of the synclinal axial surface, as discussed in text. (a) Structural measurements reported on top of Landsat images. Inset is a topographic map with contour lines every 50 m. Wind gaps are indicated by letter w. Triangular facets limit the Quilitak topographic high to the south (see also Figure 15). A steep bedding-parallel thrust fault limits Quilitak topographic high to the north. (b) Bedding dip data and topographic profiles showing that a synclinal axial surface marks the base of the fold scarp facet (see location in Figure 14a). These dips and the 31° slope of the facet are used to test the interpretation that the facet is the folded equivalent of the eroded low-relief surface to the south (see Figure 14d and Table 2). (c) Cross section based on seismic line and surface geology across Quilitak (location in Figure 14a) showing relationships between structure, surface dip measurements, and uplifted topography. The synclinal axial surface that marks the southern edge of the uplift is produced by the steepening of the dip on the back thrust. Well-imaged throughgoing seismic reflectors are shown as light lines. (d) Kink band migration model that quantitatively fits the structural measurements and observed morphology (see Table 2). Approximately 1.1 km of fault slip since topographic emergence is indicated.

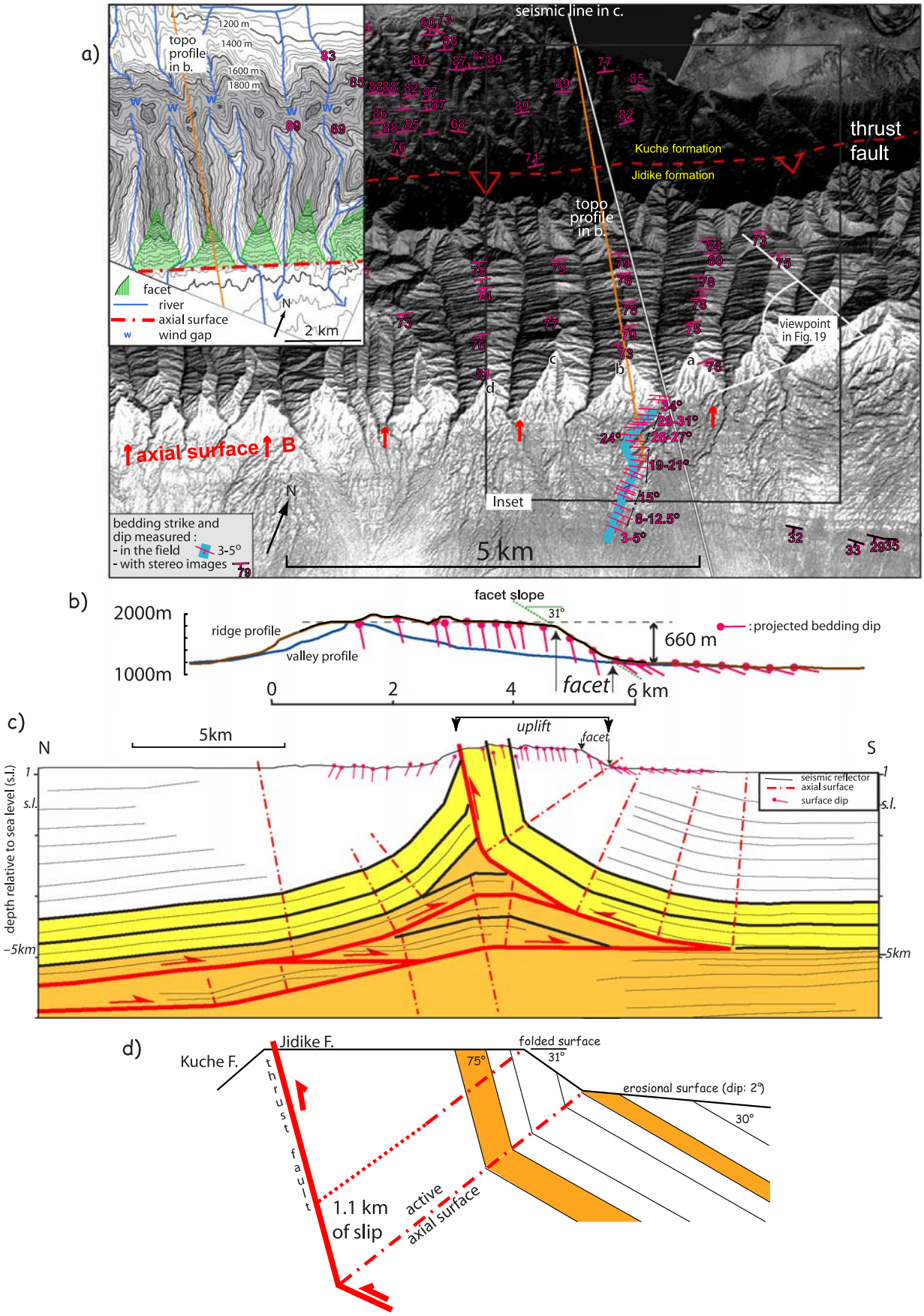
a)
topo profile in b.
1200 m
1400 m
1600 m
1800 m
facet
river
axial surface
wind gap
N
2 km
seismic line in c.
thrust fault
Kuche formation
Jidike formation
topo profile in b.
viewpoint in Fig. 19
axial surface
B
Inset
5 km
bedding strike and dip measured :
- in the field 3-5°
- with stereo images
b)
2000m
1000m
ridge profile
valley profile
facet slope
31°
660 m
: projected bedding dip
0
2
4
facet
6 km
c)
N
S
5km
uplift
facet
depth relative to sea level (s.l.)
s.l.
–5km
seismic reflector
axial surface
surface dip
d)
Kuche F.
Jidike F.
thrust fault
folded surface
31°
75°
erosional surface (dip: 2°)
30°
1.1 km of slip
active axial surface

Figure 14

alluvial conglomerates that onlap steeply dipping strata of the Quilitak ridge (Figure 12d), are presently uplifted and folded as they pass through axial surface B (Figure 13c). The dark gray conglomeratic alluvium, which visually contrasts with older steeply dipping sandstone strata, is now incorporated by uplift into the Quilitak topographic high. Its overall morphology is similar to what can be predicted by a simple fault bend fold model involving onlap of alluvium over the active axial surface (Figure 13d).

[33] The edges of the Quilitak mountainous relief can thus be interpreted as a direct surface expression of active axial surfaces bounding the anticlinal core. The morphology is consistent with the kink band migration deformation mechanism inferred for Quilitak. In fault bend folds active axial surfaces are the only locus of active deformation during earthquake rupture on the underlying thrust fault. It is thus expected that active axial surfaces have a specific morphological expression, as do faults.

[34] Even if the Quilitak topographic high is related to active differential uplift across active axial surfaces pinned to the underlying wedging structure, some active axial surfaces, like X and Y, have no obvious topographic expression. In fact, the axial surface map in Figure 12 shows that the width of Quilitak anticline at depth is up to 4 times the surface topographic width, which is only ~5 km. However, Figure 12 also highlights a close relationship between the surface shape and changes along strike of the X-Y axial surfaces. For instance, the shape of the Quilitak ridge along strike mimics changes in the deep ramp geometry. Near Kuche Tow the relief is also offset along the transverse structure. Finally, axial surface X corresponds at times to a change in the sedimentation pattern, with active sedimentation (fan deposits) to the south and some incision to the north.

[35] The fact that only some axial surfaces have a topographic signature is a result of the relative magnitude of uplift and sedimentation rates. By analogy with Yakeng, for which topographic emergence occurs only where uplift rate is greater than sedimentation rate, some active axial surfaces of Quilitak such as X and Y are continuously buried. The situation for Quilitak is somewhat different than for Yakeng, because of the contrasting folding mechanism. The Yakeng uplift rate is a direct function of the amplitude of the finite deep structure and varies smoothly across it; therefore the edge of the morphologic uplift represents a line along which postemergence sedimentation and uplift are equal. In contrast the Quilitak uplift rate is constant between axial surfaces. In addition Quilitak is a complex fault bend fold and therefore has multiple discontinuities in uplift rate related to multiple fault bends. As the uplift rate depends on the sine of the underlying fault dip, uplift rates must show substantial variation and discontinuity across the structure (see also Figure 2). In particular the changes in uplift rate related to bends in the wedging system in Quilitak core where faults are steeply dipping (60°–70°) can be at least twice as great as the uplift change related to the Quilitak ramp (20°–25° dip). Uplift discontinuities along axial surfaces related to the wedging system in Quilitak may be such that the uplift suddenly exceeds sedimentation. In contrast, uplift discontinuities related to the other axial surfaces X and Y may not be enough to exceed sedimentation, so the related axial surfaces are not apparent in the topography. Similarly axial surfaces A and B that bound Quilitak ridge start to be buried east of the East Quilitak River, as slip on the underlying thrust decreases. For example, Figure 13b highlights river pattern changes along axial surface A east of Quilitak River. The river network is no more deviated along the axial surface but simply change from aggrading to incising. As slip further decreases eastward, the whole anticline is fully covered by sediments, while active folding still occurs along active axial surfaces A and B.

4.3. Development of Large-Scale Triangular Fold Scarp Facets, Southern Front of Quilitak Anticline

[36] In this section, we further document the large-scale geomorphic effect of active axial surfaces or hinge zones intersecting the topographic surface. We focus specifically on the southern front line labeled B in Figure 12. Study of the northern Quilitak front labeled A in Figure 12a is less suitable because of erosion by rivers flowing along the topographic northern edge.

[37] The Quilitak southern front is characterized by an abrupt rise in topography and shows a distinctive faceted morphology composed of steep triangular/trapezoidal mountain front facets (Figure 3, details in Figures 14, 15, 16, and 17) separated by distinct V-shaped, "wine glass" valleys (Figures 14a and 15a) marked by incised "stems" just upstream from the mountain front [cf. *Armijo et al.*, 1986]. West of the East Quilitak River, the set of facets is continuously developed except where major river incision and erosion has occurred near water gaps (Figure 3). To the south of the facets, the topography is nearly flat or very gently dipping southward (Figures 14, 15, 16, and 17). The junction between the facets and the low dipping surface to the south corresponds to the continuous and linear front line B in Figure 12, which defines the southern edge of the Quilitak ridge.

[38] Triangular mountain front facets are usually considered the morphological signature of normal faults. They form on the footwall blocks and are marked at their base by the active fault trace. By analogy with normal fault facets, the Quilitak facet morphology (Figure 15) suggests that sustained recent uplift is occurring along the Quilitak front line. However, no active fault is observed reaching the surface at the Quilitak mountain front. What is observed is a major synclinal axial surface running at the base of the facets.

Figure 15. Views of west Quilitak triangular facets looking north. The surfaces of the ~600- to 700-m-high triangular facets are shown to be the folded equivalent of the low-relief landscape to the south in the foreground. The base of the slope is the locus of a synclinal axial surface across which there is a ~45° change in bedding dip, which predicts the observed ~31° slope of facet b (Figure 14 and Table 2). (a) Photographs. Labels b and c refer to facet labeling in Figure 14a. (b) Shaded three-dimensional (3-D) view of the Quilitak topographic high and its facets with a vertical exaggeration of two. Viewpoint is shown in Figure 3.


a)
W
E
c
b
W
E
b
c
b)
d
c
b
a
1950 m
1850
1750
1650
1550
1450
1350
1250
1150
1050
1 km

Figure 15

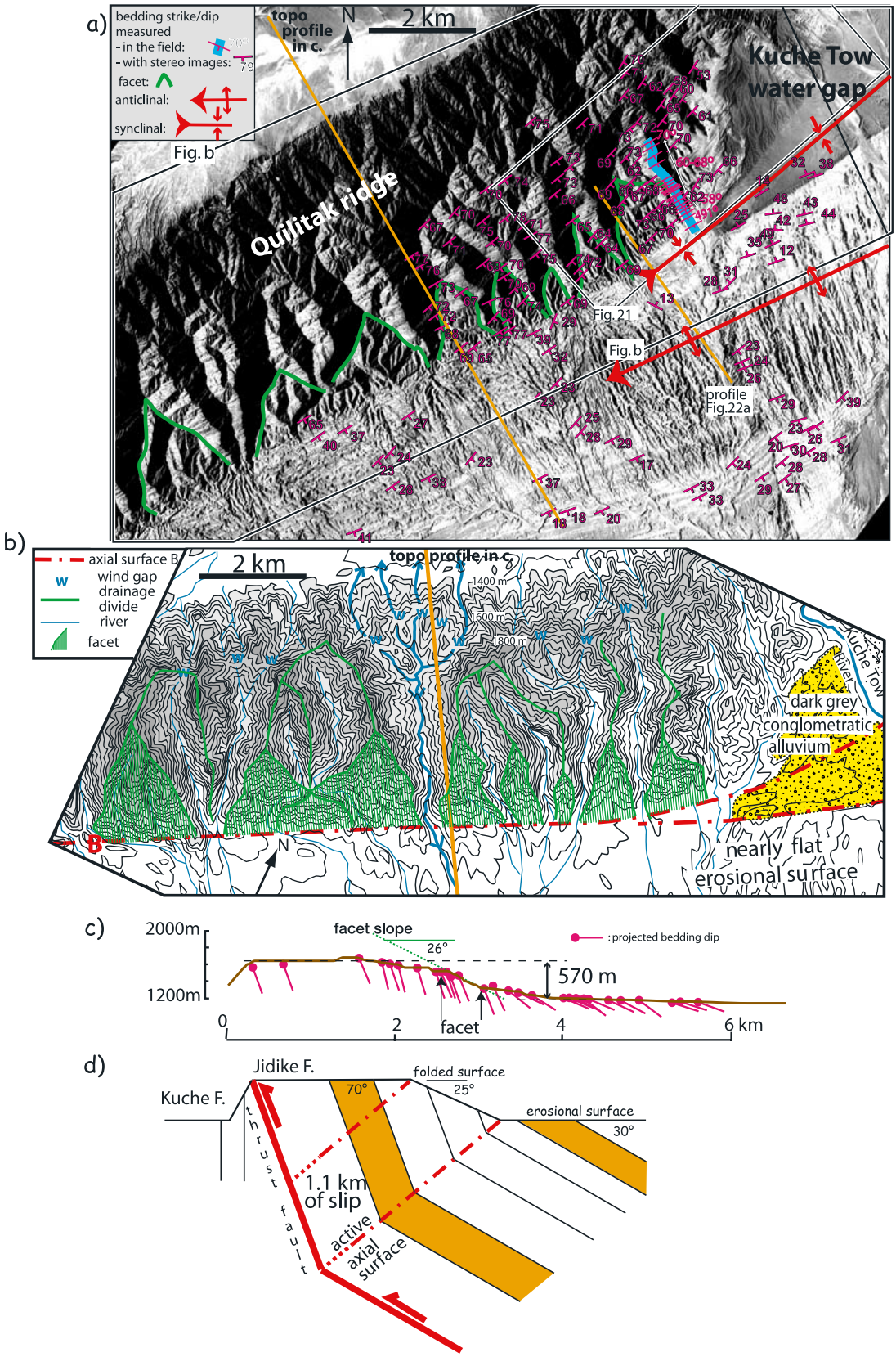
a)
bedding strike/dip measured
- in the field:
- with stereo images:
facet:
anticlinal:
synclinal:
Fig. b
topo profile in c.
N
2 km
Kuche Tow water gap
Quilitak ridge
Fig. 21
Fig. b
profile Fig.22a
b)
axial surface B
wind gap
drainage divide
river
facet
2 km
topo profile in c
1400 m
1600 m
1800 m
Kuche Tow
dark grey conglometratic alluvium
nearly flat erosional surface
N
c)
2000m
1200m
facet slope
26°
: projected bedding dip
570 m
0
2
facet
4
6 km
d)
Jidike F.
Kuche F.
folded surface
25°
70°
erosional surface
30°
thrust fault
1.1 km of slip
active axial surface

Figure 16

[39] To decipher the origin of these facets and determine their relationship with the deep structure, we examine in detail the surface structure and topography of the Quilitak southern front in three different areas: West Quilitak (Figures 14 and 15), West Kuche Tow (Figure 16), and Kuche River (Figure 17); see Figure 3 for area locations. We combine fieldwork, seismic reflection data and a stereophotogrammetry to measure bedding strikes and dips in those remote areas. Seismic reflection data particularly constrains low dips in the West Quilitak area whereas the stereo imaging method constrains high dips in all the areas (see Appendix A).

[40] Structural measurements show that Quilitak surface structure is generally similar in the three studied areas. The southern limit of the Quilitak mountainous topography (front line B) at the facet base coincides with an axial surface or hinge zone along which a sharp change in bedding dips occurs (Figure 14, West Quilitak area; Figure 16, West Kuche Tow area; Figure 17, Kuche River area). On the southern flank of the Quilitak topographic high, beds are dipping steeply southward (80°–75° in West Quilitak, 70° in West Kuche Tow, and 65° in Kuche River), whereas the nearly flat erosional surface to the south is underlain by bedding that dips 30° or less. Minor structural differences exist in the three different areas, including some secondary folding, but the base of the facets in Quilitak is always a synclinal hinge along which a change in dip of at least 35° occurs. We thus conclude that the front line B bounding the southern edge of the Quilitak topographic high (Figure 12a) is an axial surface zone.

[41] The facet morphology and ''wine glass'' canyons (Figure 15) further indicates that active uplift is occurring along the hinge zone at its base, which means that the axial surface is active. The triangular facets and the associated sudden rising in the topography attest that rocks move with respect to the axial surface and are folded as they pass through it. We thus interpret the facets as cumulative fold scarps resulting from the folding of the erosional surface to the south as it passes northward across the active axial surface by a kink band migration mechanism. On the basis of surface mapping and seismic imaging, the underlying cause of the kink band migration in this case is likely fault bend folding (Figure 14) above the thrust emerging to the north, but the analysis of the facets does not depend on any assumptions about the specific cause of the kink band migration. Fault propagation folding and some types of box folding and fold interference also drive kink band migration. However, using a simple fault bend fold model, we can match the observed changes in bedding dip, the slope of the facets and the overall Quilitak relief in the three previously studied areas: West Quilitak (Figure 14), West Kuche Tow (Figure 16), and Kuche River (Figure 17).

[42] We test the kink band migration hypothesis for the formation of the triangular facets by computing the predicted dip of the facet surface and comparing it to the observed topographic dip (Table 2). Using the changes in dip across the axial surfaces, we compute the predicted topographic inclination of the triangular facets in each of the three areas based on the assumption that it is the folded equivalent of the land surface south of the mountain front. This is computed using folding vectors assuming a flexural slip mechanism [*Shaw et al.*, 2005] or using a fault bend folding equation (see Table 2). In West Quilitak where a change in bedding dip of ~45° occurs, we predict a 31° dip for the folded erosional surface which agrees with the 31° facet topographic slope (Figure 14); in West Kuche Tow where a change in bedding dip of ~40° occurs, we predict a 25° dip for the folded erosional surface which agrees with the 26° facet topographic slope (Figure 16); and at Kuche River where a change in bedding dip of 35° is observed, we predict a 23° dip for the folded erosional surface which agrees with the 23° facet topographic slope (Figure 17). Quilitak large-scale morphology that looks like a box fold with a nearly flat top can also be reproduced using the same fault bend folding model. In West Quilitak (Figure 14) and West Kuche Tow (Figure 16), about 1.1 km of slip along the northern thrust is required to match the facet relief. The fact that the relief and the facet slopes are lower in West Kuche Tow relative to West Quilitak is related to smaller changes in bedding dips across the hinge in West Kuche Tow (Figure 16). East of the Kuche River (Figure 17) the morphology is slightly different and a much greater slip of 1.7–1.6 km is required to generate the observed topography.

[43] We have thus established a direct relationship between the southern topographic front of Quilitak and active axial surfaces related to the deep structure: the whole ridge can be approximated by a simple kink band migration model, driven by fault bend folding. The particular facet morphology also highlights the fact that active axial surfaces are significant phenomena for understanding and interpreting thrust-related active tectonic morphology.

4.4. Role of Surface Processes in Shaping Quilitak Relief

[44] The relief of Quilitak appears to result from a nonsteady competition between tectonic and geomorphic processes. The mismatch between the ~0.7–1.0 km of topographic relief of Quilitak and its 4–5 km of pregrowth structural relief (Figure 4) suggest that surface processes are on the average nearly as important as tectonics over the entire history of deformation. Erosion, combining river incision and denudation of hillslopes, tends to lower the Quilitak ridge. Furthermore, adjacent sedimentation raises the elevation of the flanks of the fold, thereby lowering the topographic relief of the central Quilitak uplift. As discussed in section 3.1 on the rate of growth of Yakeng, the long-term sedimentation rate has been quite constant since ~10 Ma [*Charreau et al.*, 2006], not showing the upward increase typical of some foreland basins. Therefore the progressive burial of the flanks of both the Quilitak and

Figure 16. Southern edge of the Quilitak topographic high, West Kuche Tow area (location in Figure 3). (a) Structural measurements mapped on top of Spot image. Triangular facets are highlighted. (b) Topography (contour lines every 50 m) with facets morphology highlighted (location in a). Wind gaps are indicated by letter w. (c) Facet dip and topographic high constrained by a topographic profile (location in Figure 16a). Structural measurements are reported. (d) Kink band migration model fitting structural measurements and observed morphology (see also Table 2).

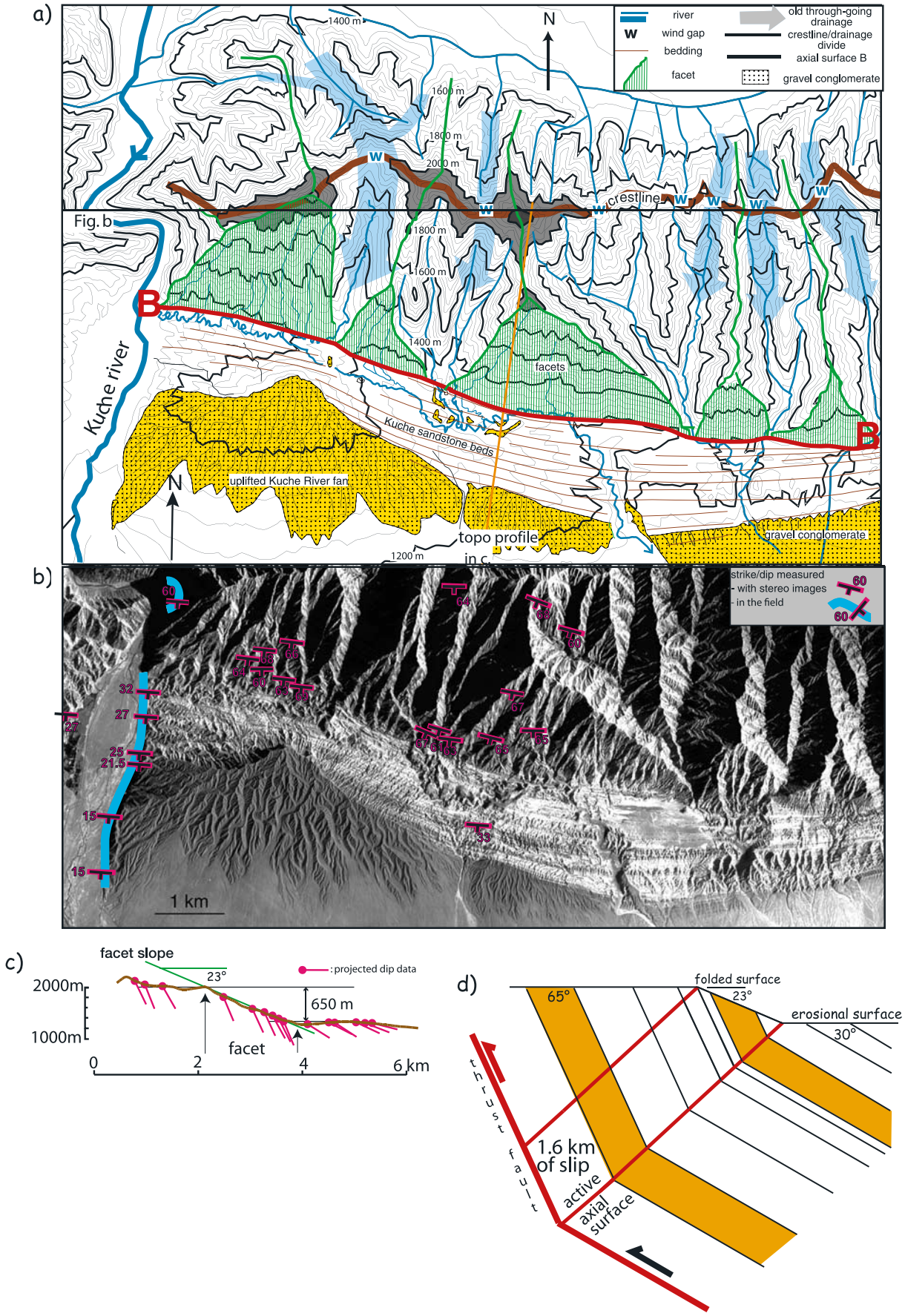
a)
river
wind gap
bedding
facet
old through-going drainage
crestline/drainage divide
axial surface B
gravel conglomerate
N
1400 m
1600 m
1800 m
2000 m
crestline
Fig. b
B
A
Kuche river
facets
Kuche sandstone beds
uplifted Kuche River fan
topo profile in c.
gravel conglomerate
b)
strike/dip measured
- with stereo images
- in the field
1 km
c)
facet slope
23°
: projected dip data
2000m
1000m
650 m
facet
0
2
4
6 km
d)
folded surface
23°
65°
erosional surface
30°
thrust fault
1.6 km of slip
active axial surface

Figure 17

Table 2. Facet Dips Computed From Structural Measurements and Compared With Observed Facet Dips[a]

	Initial Bedding Dip δ_o, deg	Folded Bedding Dip δ, deg	Axial Surface Angle γ, deg	Unconformity Dip δ_u, deg	Observed Facet Dip δ_{fo}, deg	Computed Facet Dip δ_f, deg
West Quilitak (Figure 14)	30	75	67.5	2	31	31
West KucheTow (Figure 16)	30	70	70	0	26	25
West Kuche Tow (Figure 22)	30	60	75	0	19	20
Kuche River East (Figure 17)	30	65	72.5	0	23	23

[a]Here $\cot(\delta_f - \delta_u) = [\sin^2 \gamma / \sin 2\gamma \sin^2(\gamma - \delta_o + \delta_u)] - \cot(\gamma - \delta_o + \delta_u)$, where $\gamma = 90° - (\delta - \delta_o)/2$; modified from *Suppe* [1983, equation 7].

Yakeng anticlines appears primarily to reflect a steadily rising base level of the closed Tarim basin rather than local sediment sources or basin flexure. The rise in base level is 2.4 km since the beginning of Yakeng deformation (Figure 7), which is an upper bound on the beginning of Quilitak deformation because they are linked by the same basal fault. There has been little flexure of the Kuche subbasin since the beginning of deformation [*Hubert-Ferrari et al.*, 2005a]. Therefore the basin-wide rise in base level reduces the potential topographic relief of Quilitak by 45–60% and erosion contributes another 20–35% reduction. Surface processes have thus limited the relief of Quilitak over its entire history. However, because of the steadiness of erosion/sedimentation rates, the present morphological relief still directly reflects along-strike and temporal changes in uplift rate as discussed below.

[45] In section 4.2, we have shown that west of the Kuche Tow transverse structure, differences in relief along strike between West Quilitak (Figure 14) and West Kuche Tow (Figure 16) may be related to minor changes in the axial surface geometry, and thus in uplift rate. In addition east of the East Quilitak River, the eastward decreasing Quilitak topography (Figures 3, 12, and 13) correlates with the eastward decreasing slip on the underlying ramp. Furthermore in the area between the Kuche Tow transverse structure and the East Quilitak River (Figure 3), Yakeng and Quilitak relief are anticorrelated (Figure 18), which agrees with the fact that the structures lie above the same basal thrust. West of the Kuche River Yakeng does not exist; Quilitak is the frontal structure accommodating the shortening and it reaches its highest elevation here. East of the Kuche River, Quilitak relief decreases in two steps that correspond with increases in Yakeng relief. The first ~150-m-high decrease in Quilitak relief across the Kuche River occurs where Yakeng appears. The existence of Yakeng, which accommodates part of total shortening, implies that the shortening accommodated in Quilitak must decrease. About 5 km farther to the east, the second ~280-m-high decrease in Quilitak relief and the related decrease in facet height (to less than 340 m) corresponds with the emergence of Yakeng at the surface and with an increase in its amplitude of folding at depth. East of this second step, the shortening accommodated in Yakeng is 3.5 times greater than further west [*Dittmann*, 2005], which implies again that slip accommodated in Quilitak must have decreased. The latter observations confirm that even if surface processes are dominant, Quilitak topographic relief is still a first-order record of both its geometry and of the total slip accommodated in the structure.

4.5. Topographic Emergence of Quilitak

[46] A last consideration that is important in understanding the present surface morphology of Quilitak is the recent acceleration of growth of Yakeng. Because Yakeng and Quilitak are structures linked at depth by a common detachment (Figure 4), their topographic relief must be interdependent such that the observed acceleration of growth of Yakeng will have implications for Quilitak. We consider the following two possibilities. First, acceleration of growth of Yakeng may simply reflect a decrease in the shortening accommodated in Quilitak. A second possibility would reflect an acceleration of shortening in the southern Kuche belt and thus represent a somewhat larger scale event in the Tian Shan [e.g., *Abdrakhmatov et al.*, 1996; *Burchfiel et al.*, 1999; *Burbank et al.*, 1999; *Zheng et al.*, 2000]. We favor the latter hypothesis, because a close examination of Quilitak morphology suggests that the anticline was previously buried in a way similar to Yakeng, raising the possibility that the Quilitak emergence may correlate with Yakeng emergence. Three lines of evidence suggest a relatively young emergence for Quilitak and are discussed below: (1) the triangular facets, (2) throughgoing drainage networks with wind gaps, and (3) disequilibrium ridge lines.

[47] 1. The facet morphology resulting from the folding of the pediment to the south and the existence of such an erosional surface suggest a sudden change in the fold history. This type of morphology cannot exist continuously since the beginning of Quilitak growth, ~6 Ma.

[48] 2. In the three studied areas, West Quilitak, West Kuche Tow and Kuche River, we can map valleys aligned or continuous across the anticlinal crest line that contain rivers that flow in opposite directions. Numerous wind gaps exist along the crest line, analogous to the wind gaps of Yakeng (Figures 14, 16, and 17). Valley continuity over the crest line is most striking in the West Kuche Tow area (Figure 16b). A particular drainage morphology characterizes this area. The Quilitak crest line is not centered in the middle of the 5-km-wide Quilitak relief but is lies ~4 km to the north of the southern topographic front of Quilitak. For all rivers incising the present Quilitak relief an apparent river valley can be mapped over the crest line. The most striking example is the drainage system just west of the

Figure 17. Southern edge of Quilitak topographic high, Kuche River East area (location in Figure 3). (a) Topography (50-m contour interval) with facet morphology highlighted. Wind gaps and interpreted old throughgoing drainage are indicated. (b) Structural measurements reported on top of Spot image (see location in Figure 17a). (c) Facet dip and topographic high constrained by a topographic profile (see location in Figure 17a). Structural measurements are reported. (d) Kink band migration model fitting structural measurements and observed facet morphology (see also Table 2).

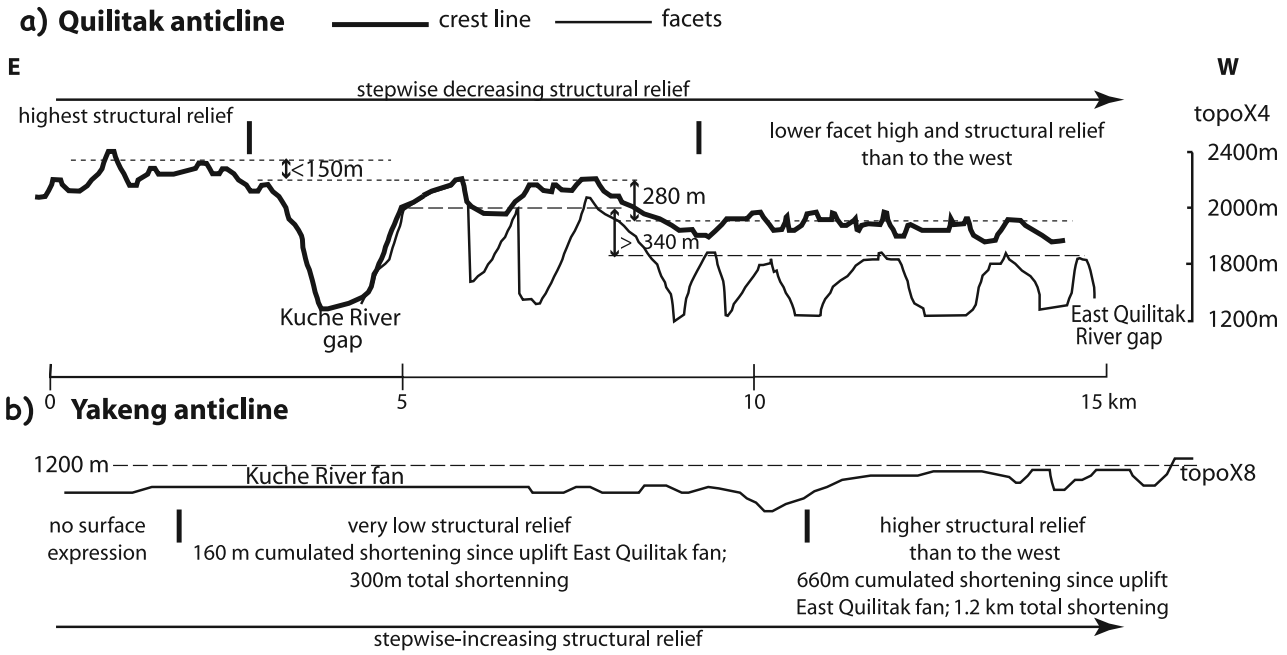

Figure 18. East-west topographic profiles (a) along the strike of the Quilitak crest line and facets and (b) along the strike of the Yakeng crest line.

topographic profile marked on Figure 16b. Without the topographic maps indicating wind gap locations, the topology of the drainage system through the structure is identical to that of a single continuous watershed with southward convergent rivers. In West Quilitak the morphology is similar with long deeply incised valleys south of the crest line and elongated ridge divides, but higher relief (Figure 14a). Therefore topographic emergence and drainage reversal in West Quilitak may have occurred earlier than in West Kuche Tow, which is consistent with the higher rate inferred across the southern axial surface in West Quilitak. In the Kuche River area (Figure 17a), relief is even higher, and the crest line is centered more on the middle of the Quilitak relief but the continuity of valleys and drainage divides across the crest line is still apparent.

[49] 3. Another indication of recent emergence or accelerated growth of Quilitak includes disequilibrium gradients of the ridgelines (Figure 19), indicating that the topography has not yet reached steady state. Modeling of *Koons* [1989] of the morphologic evolution of an eroding and uplifting fault block shows a transient memory of the preuplift flat topographic surface (Figure 19b). Koons shows that the disequilibrium is recorded in the difference between adjacent ridgeline and stream profiles. As steady state is approached the ridgeline and stream profiles become parallel. Comparison of adjacent ridgeline and stream profiles for three areas of south Quilitak (Figures 14, 16, and 17) show strongly disequilibrium profiles with the ridgeline profiles having very gentle south dipping gradients in contrast with the adjacent stream profiles for all, as summarized in Figure 19c.

[50] On the basis of the existence of throughgoing southward converging relict drainage with wind gaps and disequilibrium ridgeline gradients, we therefore conclude that Quilitak shows a recent acceleration of uplift rate similar to Yakeng anticline. Prior to this acceleration Quilitak appears have had very low topographic relief with an uplift rate in approximate balance with erosion and rise of base level, and also a throughgoing drainage network similar to present-day stream channels at the eastern end of Quilitak anticline

Figure 19. Comparison between Quilitak morphology and numerical erosion models above a block uplift done by *Koons* [1989], showing the transient topographic memory of the initially flat state before uplift. (a) A 3-D view along the West Quilitak topographic ridge looking east with the fold scarp facets to the right and the thrust fault to the left bounding the uplift (vertical exaggeration 1.5; location in Figure 14). This view, as well as Figure 19c, shows the low topographic gradients of the transverse ridges in contrast with deeply incised transverse valleys, and steep facets, similar to left-hand model in Figure 19b. (b) Numerical erosion models of *Koons* [1989] for fault-bounded block uplift of a preexisting flat surface with imposed drainage, with uplift in meters indicated. The transverse ridge line profiles initially approximate the initial flat surface so that the ridge profiles are substantially flatter than the stream profiles (model to left). All memory of the initial state is eventually erased by erosion as steady state is approached in which ridge profiles and stream profiles are approximately parallel (models center and right). Quilitak anticline approximates the transient state shown to the left. (c) Summary of topographic sections in West Quilitak (Figure 14), West Kuche Tow (Figure 16), and Kuche River (Figure 17), also showing river valley and ridge crest profiles. Subhorizontal ridge lines, in contrast with river valley profiles, indicate a topographic disequilibrium and an order of magnitude increase in deformation rate estimated at ~0.2–0.3 Ma, as discussed in text.

(Figure 20) where uplift rate must be approximately equal to rise in base level or higher if balanced by erosion. We should note that this required low preacceleration topographic relief of Quilitak anticline may not have existed for its entire early history. In particular erosion rates may not have always been enough to balance uplift rate because ~1.6 km pregrowth strata have been eroded in the core of anticline, given the observed pregrowth structural relief of

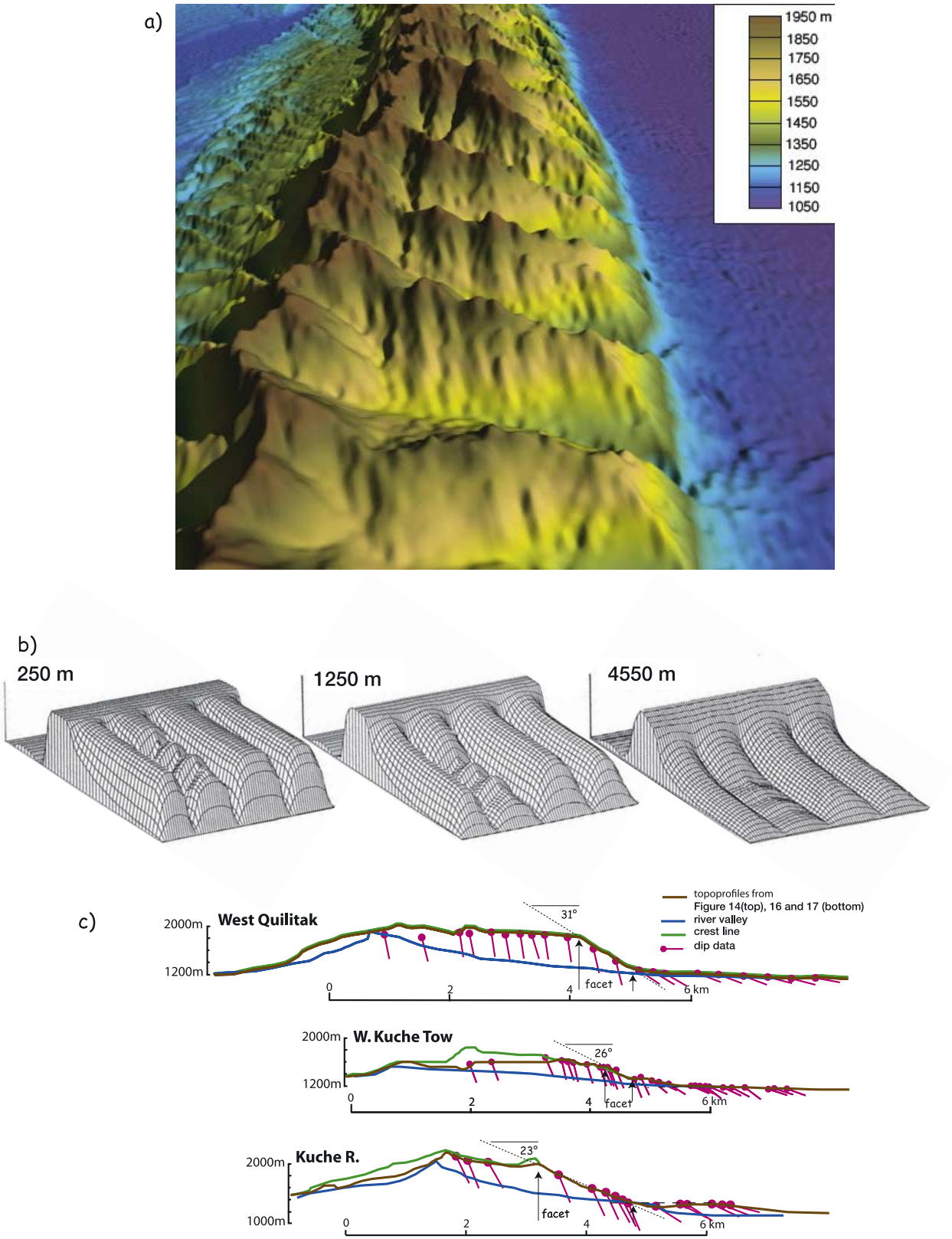

Figure 19

~5 km, a present topographic relief of ~1 km and growth sedimentation of 2.4 km.

[51] On the basis of the assumption that uplift and sedimentation were in approximate balance, the rate of preacceleration slip on the back thrusts can therefore be estimated as the long-term sedimentation rate divided by the sine of the dip of the thrust. To get a reliable back-thrust rate, we use a decompacted sedimentation rate of 0.53 mm/yr

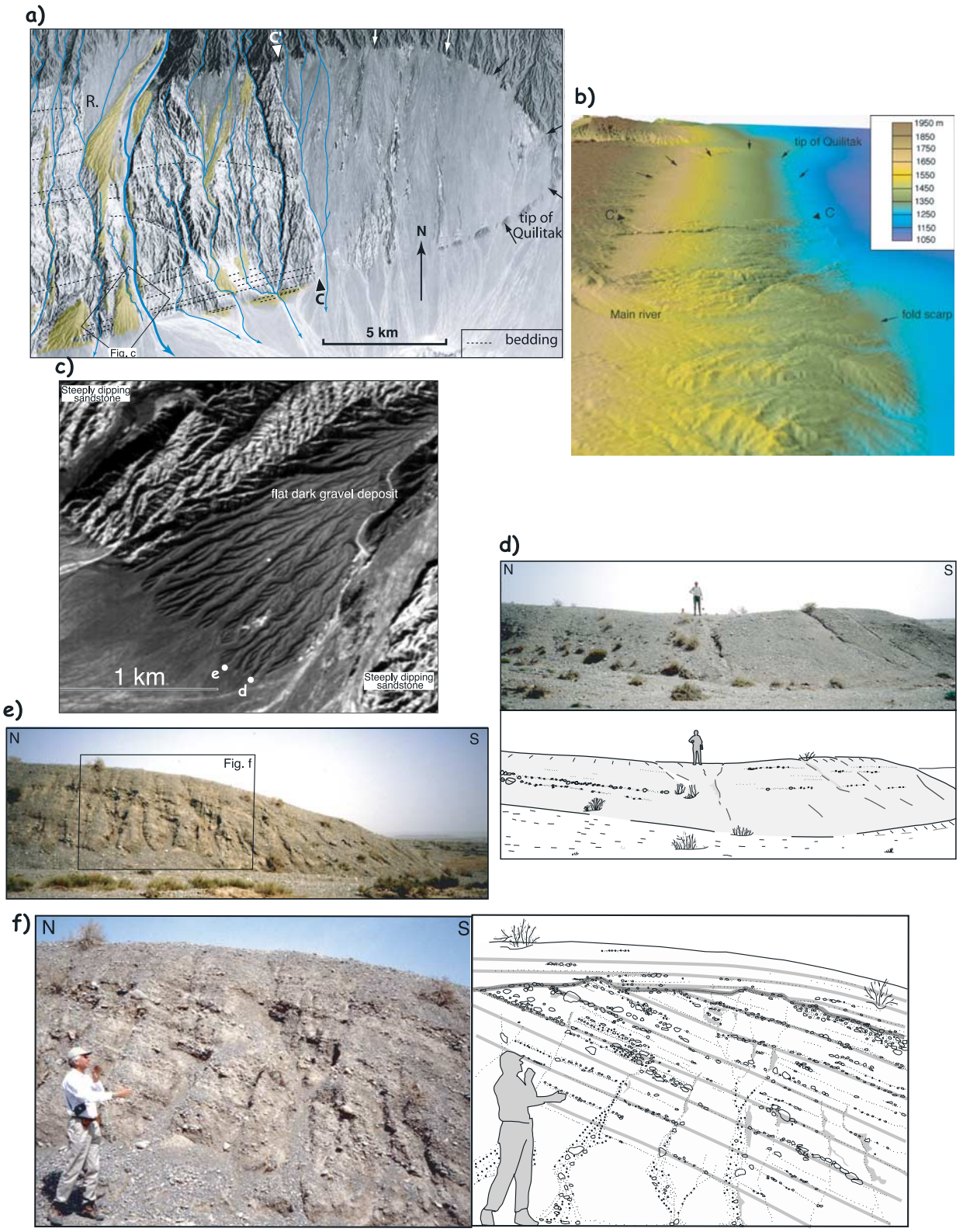

Figure 20

[*Charreau et al.*, 2006], which yields back-thrust rates of ~0.55–0.6 mm/yr for the areas of Figures 14, 16, and 17, which is a region ~50 km along strike. This rate represents a lower bound on the preemergent shortening rate because of erosion of the central uplift, discussed above. These rates, increased by ~10% to reflect slip consumed in folding on the deep ramp [*Suppe*, 1983], give a preacceleration slip rate for the deep fault of Quilitak of ~0.6–0.65 mm/yr, not including slip consumed in Yakeng.

[52] Given the observation that both Yakeng and Quilitak show an acceleration of uplift and that they are linked to the same Jidike detachment, we may use the age of emergence (160–210 ka) or acceleration (<220–280 ka) of Yakeng as an estimate of the age of acceleration of Quilitak. Given the magnitude of slip on the back thrust since the assumed time of acceleration ~220–280 ka (or later) of 1.1–1.6 km in three areas studied (Figures 14, 16, and 17), we estimate a slip rate for Quilitak of 4–5 mm/yr or greater. The accelerated rate for Yakeng in the East Quilitak section is 1.2–1.6 mm/yr. The Yakeng and Quilitak rates, even though they are both above the Jidike detachment, they cannot be immediately added because they are in different cross sections. In west Kuche (Figure 14) Yakeng is missing, at west Kuche-Tow (Figure 16) an unstudied anticline exists to the south, at Kuche River (Figure 17) Yakeng has an amplitude and total shortening that is about a quarter of the value of our studied section, and the structure is substantially different in the East Quilitak section where shortening in Yakeng is highest (Figure 4). Therefore we can estimate a total shortening rate above the Jidike detachment for the Kuche River section of about 6 mm/yr or greater, including the ~10% consumed in folding at the top of the deep ramp and based on an assumed 220–280 ka time of acceleration for Quilitak. This uncertain estimated current shortening rate is a significant fraction of the current geodetic rate across this part of the Tian Shan of 9 ± 3 mm/yr [*Reigber et al.*, 2001] and therefore suggests a significant tectonic change within the last half million years. The most proximal source of that change would be a termination of shortening consumed within the northern part of the Kuche thrust belt, which currently shows few indications of active deformation.

[53] We can test this somewhat speculative chronology for Quilitak by computing the total shortening on the deep fault, which is independently known to be ~5.5 km (Figures 4 and 14) and ~9 km near the Kuche River (Figure 12). This fault has been active since at least the beginning of growth on Yakeng anticline at 5.5 Ma. The total slip rate for Quilitak (~0.6–0.65 mm/yr) plus Yakeng (~ 1/3.5 of 0.6 mm/yr) near the Kuche River [*Dittmann*, 2005] prior to acceleration is ~0.65 mm/yr which yields a total shortening of ~3.4 km between 0.2–0.3 and 5.5 Ma. The total shortening of Quilitak along the Kuche River since acceleration is ~1.8 km and for Yakeng in the Kuche River section is ~100 m: 1/3.5 of the shortening in the East Quilitak section [*Dittmann*, 2005]. The sum of these shortening estimates for the Yakeng and Quilitak system above the basal fault since 5.5 Ma is ~5.3 km which is ~3.7 km (40%) less than the total slip on the Kuche River section on the deep ramp obtained from seismic imaging of ~9 km (Figure 12). However, it should be noted that this estimated post-5.5 Ma shortening must represent a lower bound because (1) possible contemporaneous erosion of the central uplift of Quilitak could contribute an additional 0.3 mm/yr based on the observed ~1.6 km of erosion of pregrowth strata and (2) horizontal compaction of the stratigraphic section above the Jidike detachment would contribute an additional ~2–3 km shortening over the 20- to 30-km-wide region based on observed horizontal gradients in seismic velocities south of Yakeng anticline [*see Gonzalez-Mieres and Suppe*, 2006]. The magnitude of this additional shortening associated with the erosive and compaction components is substantially uncertain, but must be within the range ~2–4.5 km. Therefore it appears, in spite of the rough nature of these estimates, that more than 80% and perhaps all of the 9 km deep slip of the Yakeng-Quilitak thrust system was consumed since 5.5 Ma when the Yakeng anticline began to grow. Therefore it is likely that this frontal thrust system of the southern Tian Shan began about 5.5 Ma and has not propagated since then. This 5.5 Ma date yields a preacceleration total shortening rate of this frontal system of about 1.3 mm/yr until the system accelerated by half an order of magnitude at about 0.2–0.3 Ma to the current rate of about 6 mm/yr.

5. Detailed Record of Deformation at a Fold Scarp Along Quilitak Southern Front

[54] In section 4 we considered the effects of kink band migration on the large-scale folding of the landscape at

Figure 20. Low-relief eastern extremity of Quilitak anticline where present uplift rate is approximately in balance with an ~0.43 mm/yr rise in base level by sedimentation on its flanks, plus any crestal erosion. This region approximates the inferred state of the present high-relief parts of Quilitak anticline to the west prior to topographic emergence at ~0.2–0.3 Ma. (a) Corona image (location in Figure 3) showing that Quilitak is not a barrier to throughgoing stream networks. West of section C-C', streams are incising sandstone/siltstone strata of Kuche/KunChung Formation [*Yin et al.*, 1998]; uplifted alluvial terraces are indicated in yellow. East of C-C', drainage is not incising, and Quilitak tip is largely buried under recent alluvial sediments, which are being folded along a fold scarp in the area of the box (Figure 20c). The main river that crosses this part of eastern Quilitak is indicated by the letter R. (b) A 3-D view of Quilitak eastern tip vertically exaggerated 1.5; viewpoint in Figure 3. (c) Corona image showing active folding along southern edge of the low Quilitak uplift. Axial surface B (Figure 12) is active, and incised flat gravel fans overlying steeply dipping sandstone beds on Quilitak ridge are folded along southern edge of the anticline, similar to the outcrop section of Figure 12d and the model of Figure 13d. White dots indicate the location of field views in Figures 20d and 20e. (d) Synclinal active axial surface at the southern edge of Quilitak ridge. (e and f) Growth unconformity similar to Figures 12d and 13d showing flat gravels unconformably on top of steeply dipping gravel beds, whereas the overlying beds become parallel to the underlying beds to the south where they are folded, which is the expected geometry for folding by kink band migration (see also folding of T horizon in Figure 27c and *Suppe et al.* [1997]).

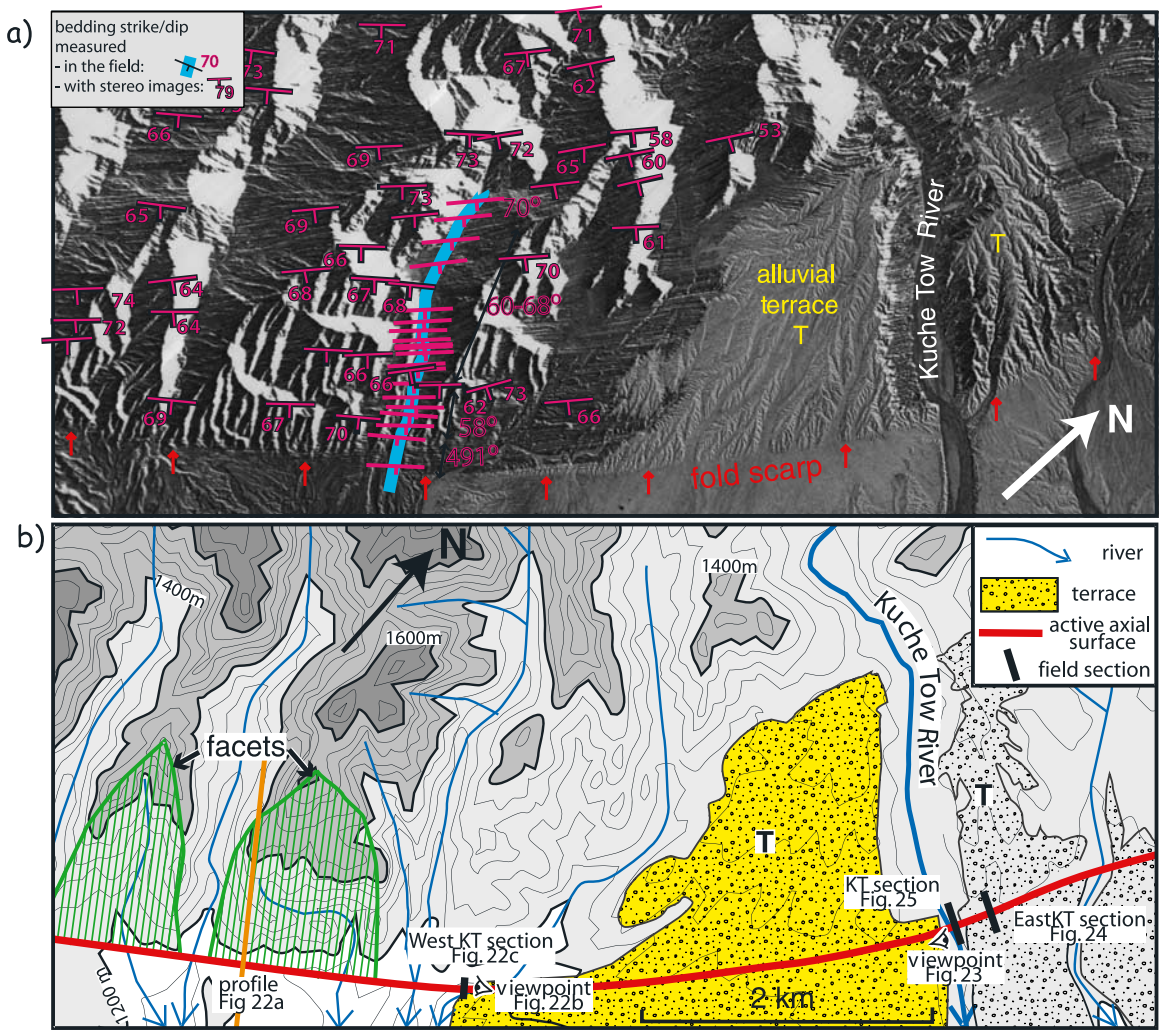

Figure 21. Fold scarp in the Kuche Tow area (location in Figure 16). (a) Corona image with structural measurements. White arrows show location of fold scarp. Folding of alluvium (terrace T) is in straight continuation with facet base to the west, indicating that it is along the same active axial surface. (b) Topographic map (50 m contour interval) with alluvial sediments mapped (dot and circle pattern) and facet morphology highlighted. Thick line indicates active axial surface along which active folding is occurring. Sections logged in the field through the fold scarp are indicated (short thick lines, see Figures 22, 23, 24, and 25).

Quilitak anticline as recorded in large triangular fold scarp facets, relict drainage networks with wind gaps and disequilibrium ridgeline profiles. Here we consider the finer-scale kinematic details of this kink band migration by defining the progressive deformation of young alluvial strata as they traverse the finite width hinge zone of the active axial surface. To do this, we must evaluate a region that has a complete stratigraphic record of deformation, which is provided by the Kuche Tow transverse structure where there is an en echelon segment of axial surface B in a small subbasin that has been characterized by rapid sedimentation where the Kuche Tow River emerges from the Quilitak mountain front (Figures 12a and 21).

5.1. Morphology in Kuche Tow: Recent Alluvium Deformed Across an Active Hinge Zone

[55] Analysis of remote sensing images shows that in Kuche Tow the main terrace level, labeled T, is uplifted and folded along a line that is in straight continuity with the active axial surface bounding the triangular facets ~5 km to the west (Figure 21). The folded terrace deposits are deposited by the Kuche Tow River, which is a small stream that has exploited the structural low created by the Kuche Tow transverse structure to cross the anticlinal high. Terrace T is composed of a few meters thick, dark gray conglomerate unit deposited above abraded yellow gray steeply dipping sandstone beds forming the bulk of the Quilitak

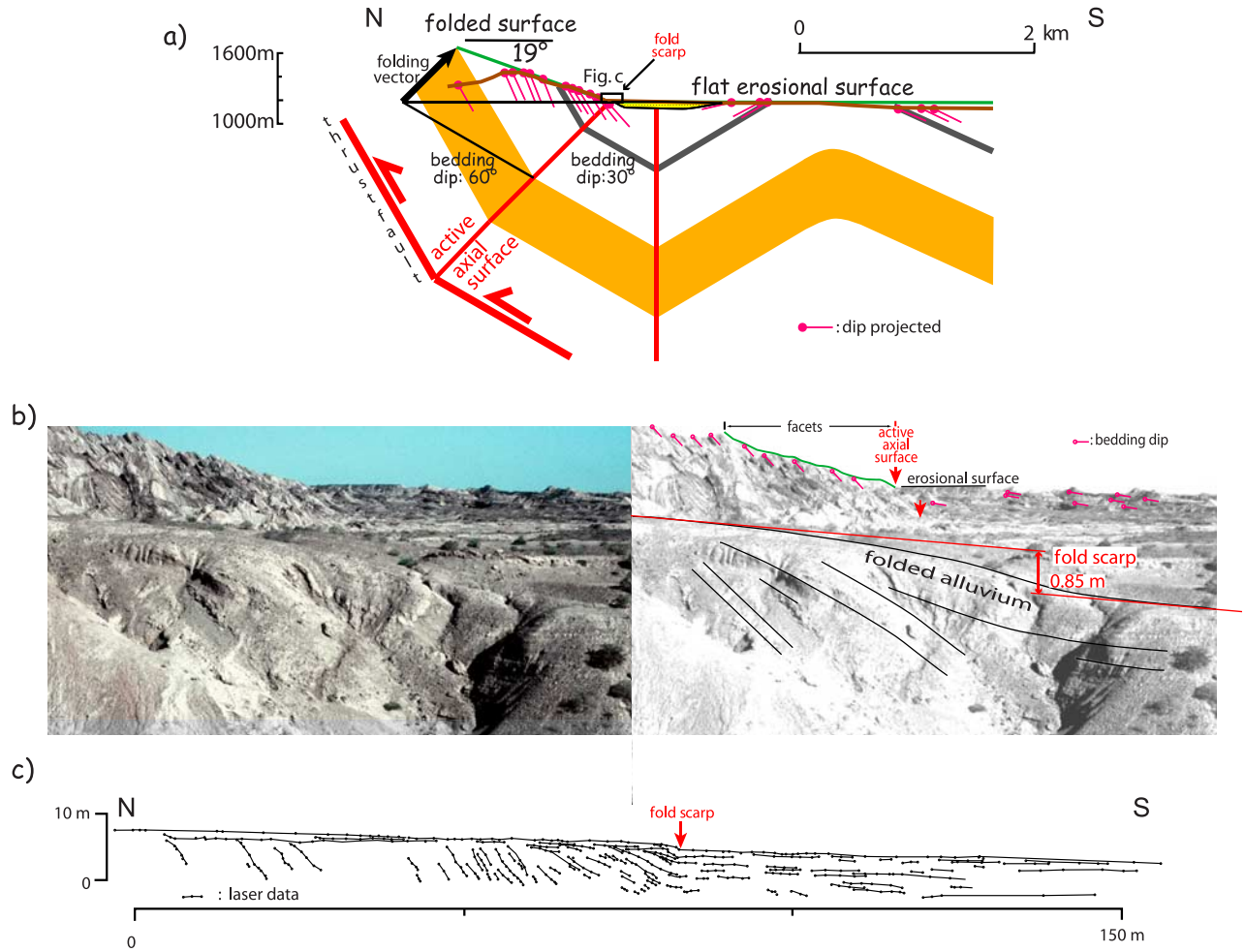

Figure 22. Folding of recent alluvium along an active axial surface, West Kuche Tow area. (a) Structural section (see location in Figures 16 and 21). (b) View to west of the 0.85-m-high fold scarp in straight continuity with axial surface at large-scale facet base, which is seen in profile on the horizon. (c) Surveyed field section West Kuche Tow at the location in the foreground of Figure 22b, showing the hinge zone in young alluvial sediments underlying the fold scarp, with progressive folding.

southern limb. The folding of terrace T is not only visible in remote sensing (Figure 21a), but is also exposed for detailed examination in several incised valleys: (1) the West Kuche Tow section (Figure 22) near the western limit of the T terrace close to the triangular facets and (2) the Kuche Tow and East Kuche Tow sections (Figures 23, 24, and 25) along the Kuche Tow River (see Figure 21b for locations). Both incised valleys show the progressive folding of young strata which we show to fit the predictions of kink band migration (Figures 26 and 27).

[56] In the field photograph of Figure 22b, we see in profile in the background the facet to the north, the erosional surface to the south and the sudden intervening change in bedding dips at the axial surface. In the foreground folding of recent alluvium of the westernmost development of terrace T results in a 0.85-m-high fold scarp. The cross section measured in the streambed below the fold scarp (Figure 22c) further shows that surface folding occurs right at the synclinal hinge where the bedding dip changes from 0 to 60°.

[57] The morphology in Kuche Tow thus shows that recent Quaternary alluvial sediments are uplifted and folded along an active axial surface or hinge. The fold scarp formed in this way records the most recent uplift of the steeply dipping core of the Quilitak anticline along active axial surface B (Figure 12a). The 0.85-m-high fold scarp in Figure 22c is indeed likely to represent incremental instantaneous folding across an active axial surface because alluvium deposited in front of the axial surface would roll through the hinge during an earthquake rupture on the underlying thrust. Farther east, the fold scarp across the main terrace T is higher (Figure 23) and represents cumulative folding across the active hinge. As active sedimentation occurs south of the fold scarp, the apparent scarp height across T is only produced by folding since river incision and is not the total deformation of the terrace. Just north of the scarp, flat-lying alluvial beds lie unconformably over ~55° southward dipping sandstone beds (Figure 23). This pattern of deformation is expected because the alluvium deposited beyond the active axial surface would never be folded and will remain flat-lying [*Suppe et al.*, 1997]. The

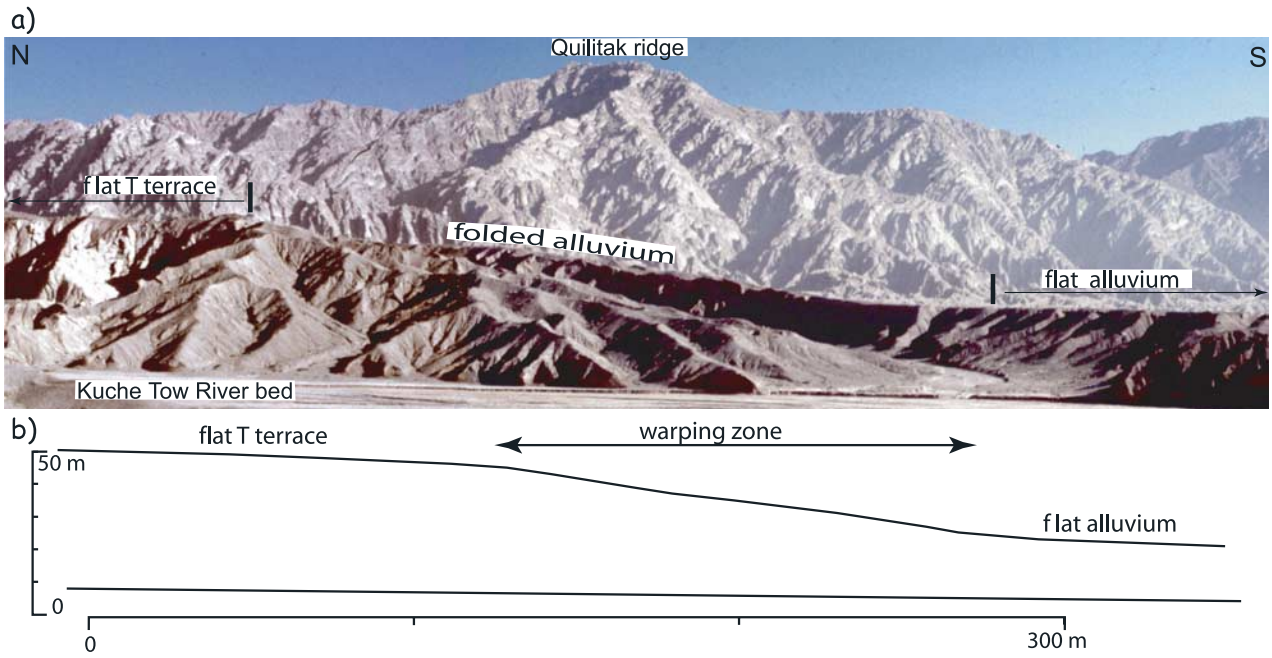

Figure 23. Large-scale fold scarp east of the Kuche Tow River (location in Figure 21). The underlying structure and stratigraphy show that the folded surface is not a single preexisting terrace; rather the flat alluvium to the south is much younger than the uplifted flat T terrace to the north (see Figure 27c and text). The fold scarp records the total postincision deformation of a previously flat landscape. (a) View to east of postincision fold scarp. (b) Topographic profile across the preincision surface showing that warping occurs over a 100- to 200-m-wide zone.

horizontal nature of these beds also indicates that the component of large-scale limb rotation is negligible.

5.2. Quantitative Measurements of Folding Across an Active Hinge Zone

[58] In order to better understand the folding processes across active hinges and the interaction between deformation and sedimentation, we logged structural sections across the fold scarp in natural river cuts. We measured three sections (locations in Figure 21). One is located along the Kuche Tow River (Kuche Tow section, Figure 25), the next one is ~100 m more to the east (East Kuche Tow section, Figure 24), and third one along a small river channel at the western extremity of terrace T about 3 km west of the Kuche Tow River (West Kuche Tow section, Figure 22b). The cross sections provide a bed-by-bed image of the folding process in the hinge zone.

[59] In each river cut we use a combination of laser surveys and digital photographs to map the variation in bedding shape in the hinge zone. Laser surveys allow us to obtain an undistorted view of the growth structure in cross section that was not possible with only outcrop photographs. The intrinsic precision of the instrument we used and the length of the section (<300 m) ensure that instrumental errors are a few tens of centimeters at most. The primary uncertainty comes from identifying the stratal continuity of a bed during laser surveying. To increase our accuracy, we measured bed shapes on both sides of the river channel when possible and created a composite cross section by stacking them. Finally, data are projected into cross sections (Figures 22c, 24b, and 25b) that are perpendicular to the strike of the active hinge.

[60] All the sections show a progressive decrease in bedding dip from 50°–60° in the north to flat in the south. Dip changes occur over a distance of about 200 m in the Kuche Tow and East Kuche Tow sections, and over a much shorter distance, ~25 m, in the West Kuche Tow section. Therefore the changes in dip do not occur abruptly but are distributed across a hinge or axial surface of finite width along which progressive folding occurs [*Suppe et al.*, 1997]. A distinct synclinal hinge is present in all sections, which marks the beginning of active folding and thus the entrance of strata into the hinge zone. North of the synclinal hinge, beds become progressively more folded northward until a dip that is conformable to the dip of the steep south limb of the Quilitak core is attained. The process is best recorded in the Kuche Tow and East Kuche Tow sections that have the greatest width and vertical depth of exposure. We will thus mostly focus on those areas.

[61] In the Kuche Tow (Figure 25) and East Kuche Tow (Figure 24) sections, a key horizon is the dark gray fanglomerate of the uplifted T horizon and the underlying erosional surface. North of its anticlinal hinge the T horizon has a flat dip and unconformably overlies 56° dipping yellow gray sandstone beds similar to the present Tarim sediments (Figures 24 and 25). South of the anticlinal hinge the T horizon has a ~30° dip, with overlying alluvial beds having slightly gentler dips and underlying sandstone beds slightly steeper dips. Furthermore, above the ~30° dipping T horizon changes in bedding dip appears to be quite gradual, whereas below the T horizon changes in bedding dip are more abrupt with distinct angular disconformities or unconformities. The latter attest to frequent episodes of nondeposition or minor erosion north of the hinge zone

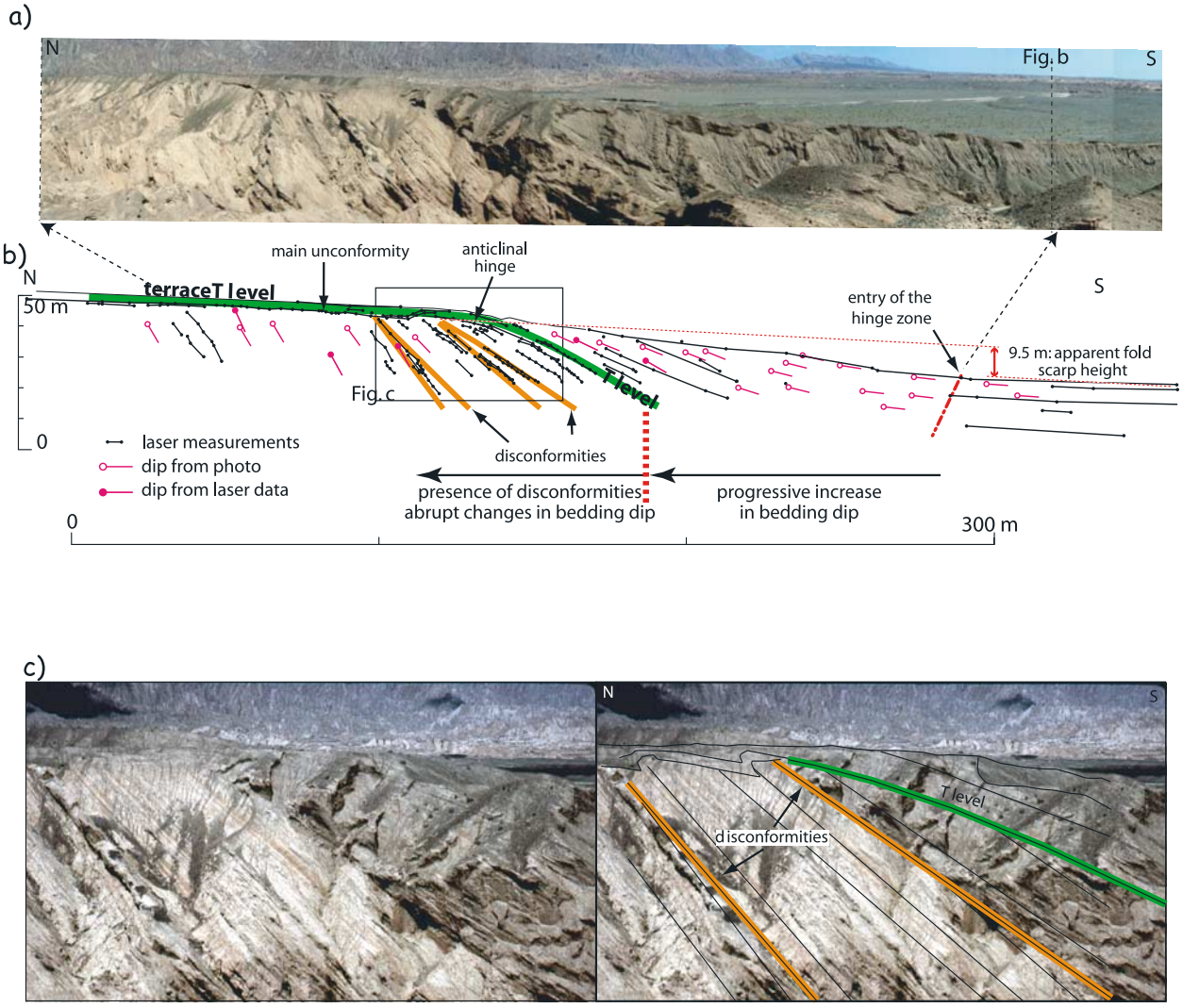

Figure 24. Main East Kuche Tow River section through the folded preincision surface (see location in Figure 21), approximately 100 m east of Kuche Tow River and section in Figure 25. (a) View of progressive changes in bedding dip below folded preincision surface. Note that this preincision surface is not a single terrace. The uplifted T terrace level corresponds to an intermediate level within the stratigraphic section approximately 50 m below the level of the incised terrace south of the fold scarp. (b) Section measured with a laser. (c) View of sharp disconformities occurring below terrace T level.

prior to the deposition of the T horizon. In contrast the gradual decrease in dips without distinct angular disconformities or unconformities attests to a slightly higher sedimentation rate during folding after the deposition of the T horizon. The bedding pattern in the Kuche Tow wide hinge zone thus suggests fine interaction between tectonics and erosion/sedimentation in shaping bed geometry within active hinge zones, which we explore in more detail below.

5.3. Kinematics of Folding Processes Across a Wide Active Hinge Zone

[62] To understand in a more quantitative way the observed bedding geometry in the hinge zone, we model the folding processes involved and their interaction with sedimentation using hinge zone migration theory [*Suppe et al.*, 1997]. Large-scale fault bend fold models such as in Figure 14 cannot account for the progressive changes in dip observed in the hinge zone area over distances of up to hundreds of meters. Such models have sharp hinges of zero width. Sharp hinge fault bend fold models were built to approximate the behavior of large-scale structures where hinges are narrow relative to limb width and limb dips are relatively constant over large regions. To account for folding processes at the bed-by-bed scale, *Suppe et al.* [1997] simply proposed to expand the sharp axial surface line used in fault bend folding to be of finite width, bounded by entry and exit axial surfaces (Figure 26a). Within the wide axial surface zone, the bedding dips would change gradually in a rounded hinge zone of given width, and the local kinematics would be similar to curved similar folding.

[63] The kinematics of this balanced forward model of growth folding is illustrated in Figure 26. We use a steady

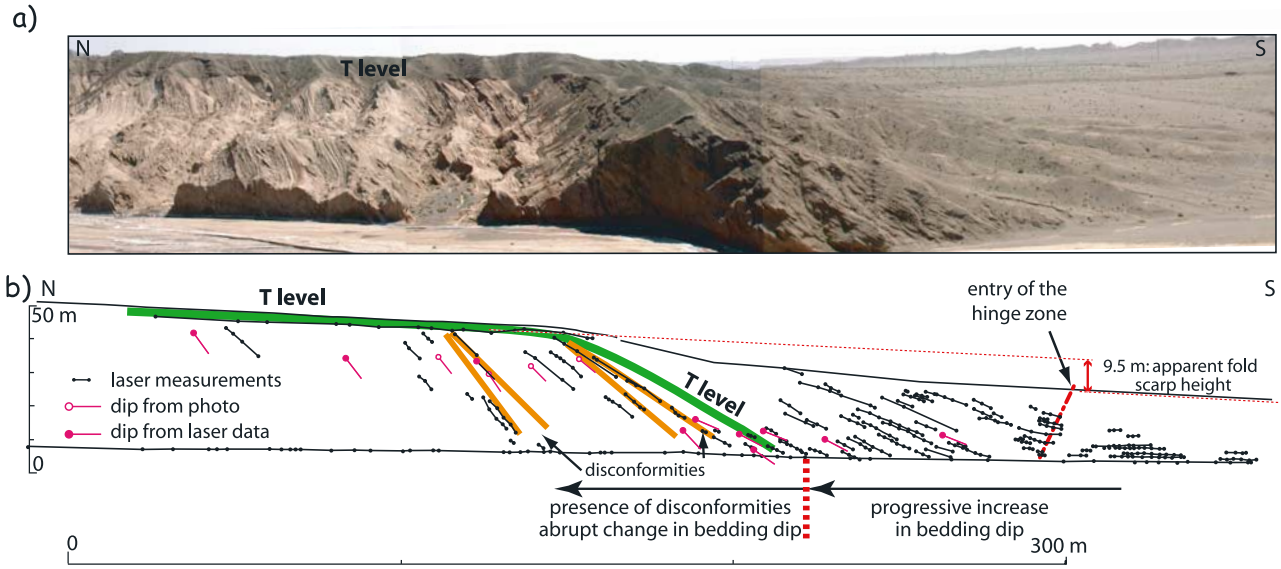

Figure 25. Kuche Tow River section through the folded preincision surface (see location in Figure 19), approximately 100 m west of the section in Figure 24. (a) Views of progressive changes in bedding dip below folded preincision surface. Note that this preincision surface is not a single terrace. The uplifted T terrace level corresponds to an intermediate level within the stratigraphic section approximately 50 m below the level of the incised terrace south of the fold scarp. (b) Section surveyed with a laser.

sedimentation rate relative to deformation to get an initial picture of the behavior. This model has a substantially higher ratio of sedimentation to deformation than the folds in Kuche, which allows us to illustrate more clearly the progressive folding that takes place as beds traverse the hinge zone. In this wide curved hinge model, as in sharp hinge models, sediments that are deposited in front of the active hinge (i.e., particles 1 to 6 in Figure 26) will move through it and be folded to a dip equal to the pregrowth fold limb dip once they exit the hinge zone. As hinge zones can be 10–100 m wide, which is an order of magnitude greater than characteristic 1–10 m slip in a single large earthquake, sediments will pass progressively through the active hinge zone and will be gradually folded (like particles 1 to 6 in Figure 26b which are deposited in front of the hinge zone). Sediments will be fully folded only once they have crossed the whole hinge zone (like particles 1 to 6 Figure 26c), which may take 10,000 to 100,000 years (see particle 5 in Figure 26d). Finally, sediments deposited beyond the hinge zone (like particles 8 to 9 in Figure 26) will not be folded, and sediments deposited over the hinge zone (like particle 7 in Figure 26) will be only partly folded.

[64] This active curved hinge kink band migration model yields progressive changes in dip across the fold scarp as observed in the field, and also a gentle fold scarp surface slope if ongoing sedimentation occurs. Indeed when an earthquake rupture occurs on the deep thrust related to the hinge zone, the sediments deposited above the hinge zone, or just in front of it, will be instantaneously folded to a gentle dip that is a function of how much of the hinge zone they have traversed. As deformation accumulates, as a result of more earthquakes, the sediments move farther through the hinge zone and become progressively more folded. Nevertheless, if new sediments are deposited on and in front of the hinge zone, very gentle bedding dips next to the entry axial surface are produced similar to what we observe in Kuche Tow (Figures 22b and 23).

5.4. Modeling Data From Active Wide Hinge Zones

[65] We use the balanced wide hinge kink band migration model described in section 5.3 to quantitatively analyze sections logged in the Kuche Tow area. For that purpose, a composite section was first built by stacking together bedding data from the nearby sections at Kuche Tow (Figure 25b) and East Kuche Tow (Figure 24b), which are separated by ~100 m. This gives us a greater vertical extent to the section (40 m). Then we fit the wide hinge model to the composite section. The West Kuche Tow section (Figure 22b) is less suitable because of its limited vertical extent (7 m).

[66] To get the appropriate hinge zone model for the Kuche Tow fold, we build a dimensionless forward model of growth folding with a total change in bedding dip across the hinge zone that matches the observed change in dip of 56°. We choose an arbitrary simple curved hinge zone geometry, which is the geometry that would exist in pre-growth, fully folded strata. Our choice is similar to common upper crustal hinge zone geometries [cf. *Suppe et al.*, 1997]. This hinge zone geometry represents the trajectories of all particles through the fold in self-similar kink band migration (Figure 27a). On the basis of these trajectories we compute, using folding vectors, the unique sequence of dimensionless fold shapes that all layers undergo for incrementally increasing displacements through the hinge zone. We start the computation by placing an undeformed flat horizon across the hinge zone and then track the motion of the particles that compose that horizon as they move progressively along the trajectories. By this process, we obtain Figure 27a, which

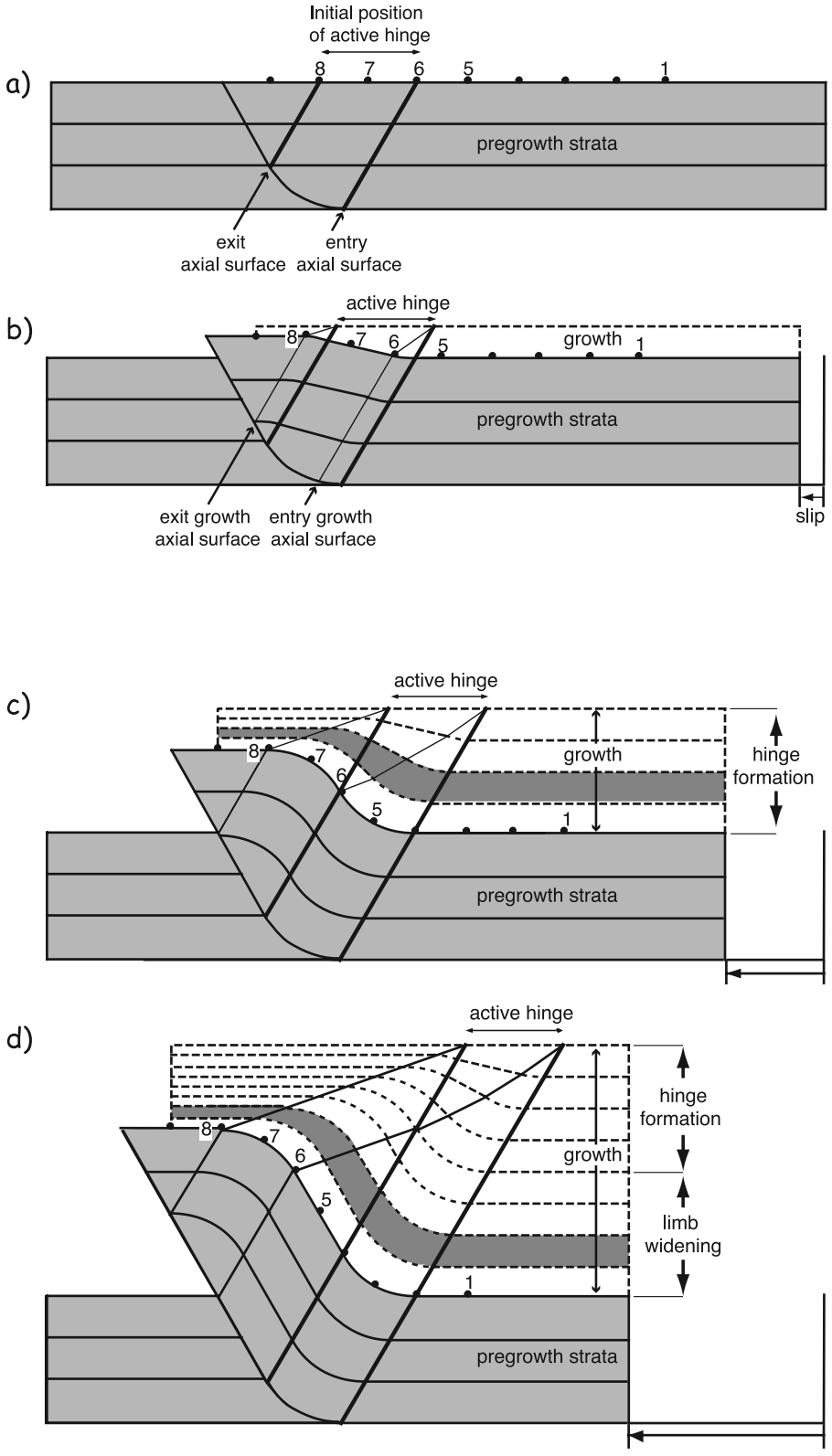

Figure 26. Progressive folding by kink band migration through a rounded hinge zone of finite width [*Suppe et al.*, 1997]. Sedimentation rate is steady; wide axial surface zone is modeled like a curved similar fold. See text for discussion of the progressive folding.

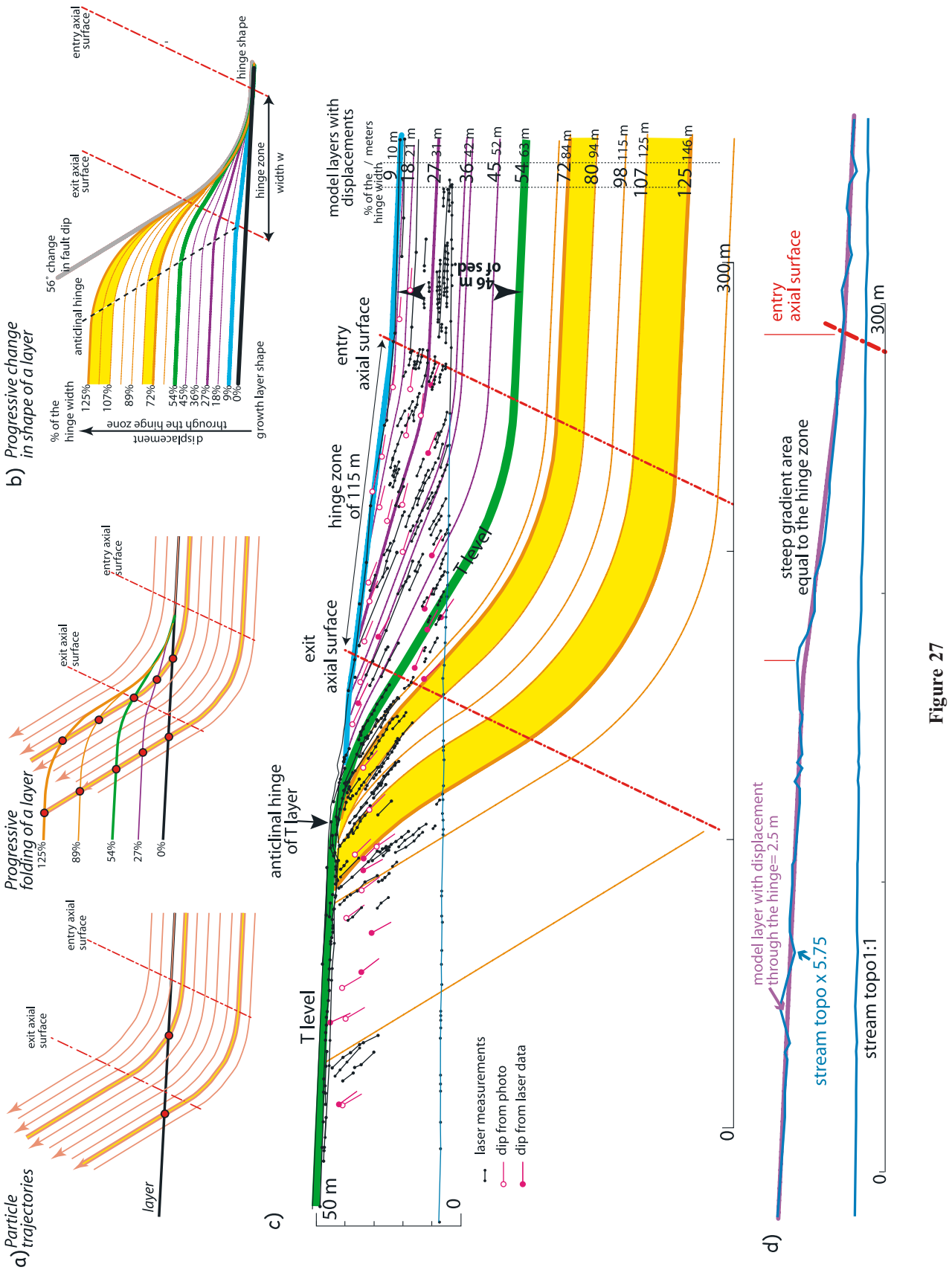
a) Particle trajectories
exit axial surface
entry axial surface
layer
Progressive folding of a layer
125%
89%
54%
27%
0%
b) Progressive change in shape of a layer
% of the hinge width
125%
107%
89%
72%
54%
45%
36%
27%
18%
9%
0%
displacement through the hinge zone
growth layer shape
56° change in fault dip
antiklinal hinge
exit axial surface
entry axial surface
hinge shape
hinge zone width w
c)
T level
50 m
0
anticlinal hinge of T layer
exit axial surface
hinge zone of 115 m
entry axial surface
model layers with displacements
% of the hinge width / meters
9 10 m
18 21 m
27 31 m
36 42 m
45 52 m
54 63 m
72 84 m
80 94 m
98 115 m
107 125 m
125 146 m
46 m of sed.
T level
300 m
0
laser measurements
dip from photo
dip from laser data
d)
steep gradient area equal to the hinge zone
entry axial surface
model layer with displacement through the hinge= 2.5 m
stream topo x 5.75
stream topo1:1
300 m
0

Figure 27

shows the set of evolving shapes of growth layers for increasing fractional displacement through the hinge zone.

[67] We then scaled our template of dimensionless fold shapes to the observed cross section. First, the modeled synclinal entry axial surface is fixed to the observed location of the entry axial surface where beds enter the synclinal hinge (Figure 27b). The model is then scaled to fit the anticlinal hinge shape of the strath base of the T horizon. The model horizon that fits the observed ~30° limb dip of the T horizon has a horizontal displacement through the hinge zone of 54% of the hinge zone width. Once the model scaling is done, the hinge zone width is fixed by the shape and location of the T horizon relative to the entry axial surface. The final step is fitting the sequence of computed horizon shapes of the now-scaled hinge zone model to the sequence of layers above and below the T horizon such that there is a monotonic upward decrease in displacement through the hinge zone. The final result is a cross section composed of the data plus the fit model horizon geometries for which the fractional displacements are all known (Figure 27b).

[68] The resulting best fitting wide hinge model can be directly compared to the dip data in Figure 27c. The agreement is striking. The first direct output of the wide hinge model is the ~115 m width of the hinge. Indeed bedding dip data in the logged sections cannot be used to directly resolve the hinge width, because only the location of the entry axial surface is directly observed and not the exit axial surface. The width and location of the hinge inferred is equal to the area of steep gradient along the river profile in Figure 27d. The stream profile thus appears to record the area of active uplift which is limited to the hinge zone area. The wide hinge model also provides a measure of horizontal displacement for each horizon. For example, it implies that the T horizon has moved through 54% of the hinge zone or 63 m northward with respect to the entry axial surface (Figure 27b). Similarly, the stream gradient can be approximated with a curve representing a displacement of 2.5 m through the hinge, which is the expected displacement in one or two large earthquakes. Finally, if we date key horizons, the hinge model will provide horizontal displacement rates of the axial surface and of any fault at depth to which it is pinned.

5.5. Interactions of Deformation and Sedimentation Across an Active Wide Hinge Zone

[69] The hinge zone model further shows that until recently the fold scarp had nearly no topographic expression. The T horizon has been buried over the hinge zone by ~46 m of alluvial sediments. However, there appears to have been little or no deposition north of the active hinge because of the relatively uniform residual thickness above the strath at the base of the T horizon, which is exposed over a wide region (Figures 21, 24, and 25). Furthermore the present topographic slope of the fold scarp (Figure 23) does not correspond to a given folded sediment layer, but is the composite result of successive onlaps of the transient fold scarps by younger sedimentary layers (Figure 27b). The scarp slope is thus a time-transgressive disconformity surface [cf. *Suppe et al.*, 1992, 1997]. Finally, the shape of the present-day fold scarp can be approximated by a deformed horizon that has moved 10 m through the hinge zone, a distance that represents 4–10 large earthquakes. We thus interpret the scarp topography as a disconformity that was nearly flat across the present fold scarp before accumulating a displacement of 10 m. The present fold scarp started to form most probably during the latest incision episode along the Kuche Tow River, which marks the end of active sedimentation in the small basin south of the fold scarp.

[70] The wide hinge model also reveals marked changes in sedimentation and erosion rates. The presence of multiple disconformities below the T horizon in contrast with their absence above the T horizon already suggested qualitatively that an increase in sedimentation rate occurs after the deposition of the T horizon. Using the wide hinge, model we can determine the ratio of tectonic deformation to sedimentation rate. We plot for each of the fitted horizons their cumulative horizontal displacements relative to their cumulative sediment thickness (Figure 28). Cumulative horizontal displacements are an output of the fitted curved hinge model (Figure 27) and the cumulative sediment thickness is obtained from the field section and from fitting deeper horizons. For example, the T horizon has a cumulative displacement of ~63 m and is buried under ~46 m of sediments. The displacement versus sedimentation graph in Figure 28 obtained in this way shows two episodes of relatively constant ratios of sedimentation to displacement with two major changes in sedimentation rate: one at the time of the deposition of the T horizon and the second more recently when the present river valley was incised and sedimentation stopped. The following scenario is thus confirmed. Before the deposition of the T horizon the sedimentation rate was lower that the uplift rate across the hinge zone. After the T horizon sedimentation rate was very slightly greater than the uplift rate and the fault scarp was buried, but the top of the T horizon was not. Most recently

Figure 27. Modeling of Kuche Tow field sections using a curved hinge kink band migration model. (a) A dimensionless wide hinge zone model for changing horizon shape with increasing fractional displacement through a hinge zone with a total change in dip of 56°, which corresponds to the observed change in dip at Kuche Tow. Gray lines indicate trajectories of particles through the fold, which are simply parallel to the bedding in fully folded strata. (b) Dimensionless templates of fold shapes for incrementally increasing displacement through the hinge. Hinge zone is bounded by entry and exit axial surfaces with an arbitrary width w. (c) Best fitting wide hinge model scaled to the Kuche Tow field sections according to the observed locations of the anticlinal hinge of T layer and the dip of the folded T layer and of the location of the entry axial surface. Each fitted bed has an associated fractional and linear displacement through the hinge zone, which gives the deformation history shown in Figure 28. See text for full discussion. (d) Best fitting location of the active hinge zone from Figure 27c correctly predicts the observed location and width of the steepened stream profile. The best fitting shape to the stream profile indicates a horizontal displacement of 2.5 m, which is equivalent to 1–2 major earthquakes.

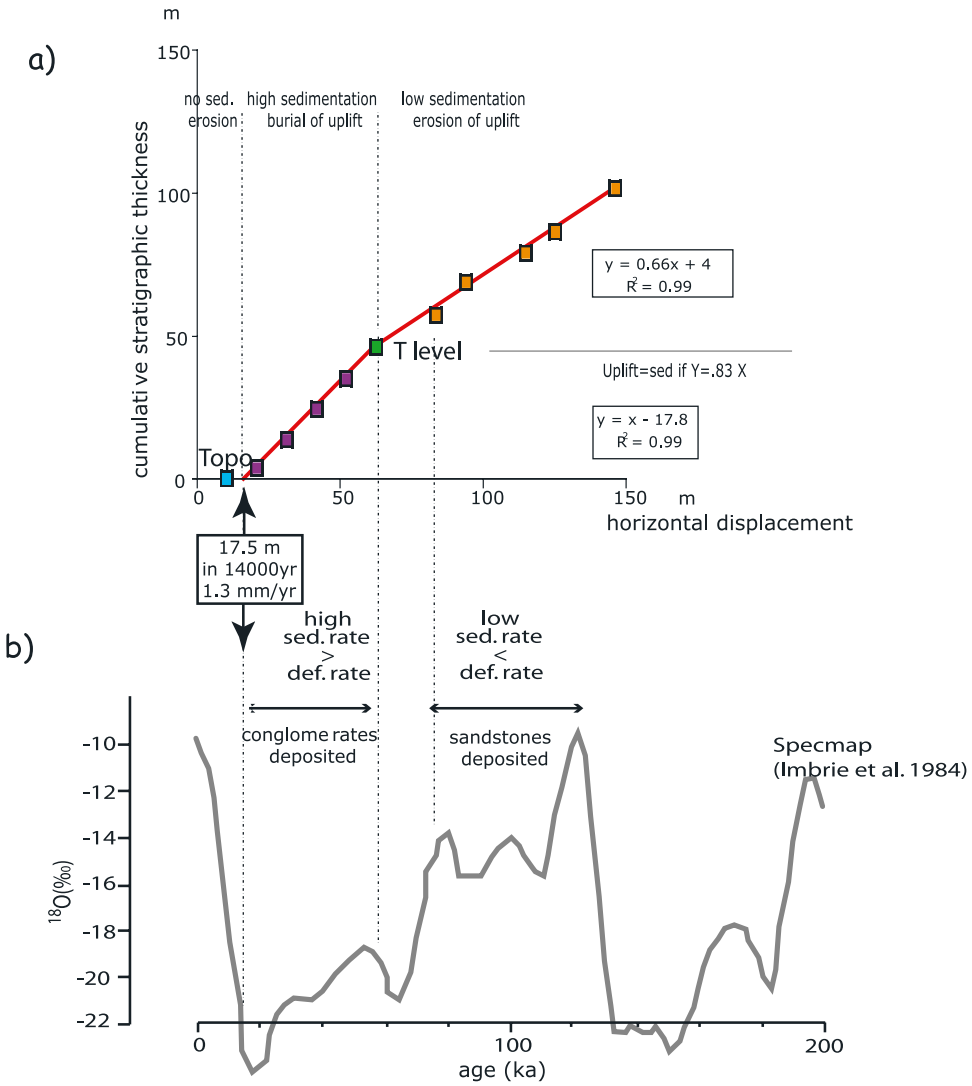

Figure 28. History of horizontal displacement through the Kuche Tow River fold scarp as a function of cumulative sedimentation. (a) Cumulative stratigraphic thickness versus horizontal displacements through the fold hinge from Figure 27c. Uplift equals sedimentation if cumulative stratigraphic thickness is equal to horizontal displacement times 0.83 = sin 56°. The period before the deposition of the T horizon shows an uplift rate slightly higher than sedimentation rate, in agreement with the observed minor growth angular disconformities and unconformities (Figures 24b, 24c, 25b, and 27c). The period after the deposition of the T horizon and before postglacial river incision shows an uplift rate that is slightly lower than sedimentation rate, with a constant ratio sedimentation rate to displacement rate. (b) Possible correlation with long-term climatic variations, as illustrated by δ^{18}O variation [*Imbrie et al.*, 1984].

sedimentation has stopped as a result of incision. A similar incision episode is present all over the Tian Shan range and may be related to climatic changes at the beginning of the Holocene (~12 ka) [*Poisson and Avouac*, 2004; *Hubert-Ferrari et al.*, 2005b].

[71] We have no direct constraints on the age of the fitted horizons at Kuche Tow yet we can propose a plausible correlation with major climatic change. If the latest incision episode indeed occurs in the early Holocene, the latest sedimentation episode may be correlated with the end of the last glacial period (18–16 ka). This correlation yields a deformation rate of ~1.25 mm/yr. This rate would yield an age of ~8 ka for final cessation of sedimentation as a result of incision, based on the 10 m of displacement since incision. Taking this constant deformation rate, we can infer the possible age of all the other horizons based on an assumption of constant deformation rate and check if there is any possible correlation between associated change in sedimentation rate with glacial/interglacial periods as defined by variation in δ^{18}O [*Imbrie et al.*, 1984]. Figure 28 shows that our correlation implies that layers above the T horizon were deposited during the last main glacial period characterized by low δ^{18}O, whereas layers below the T horizon were deposited during the last interglacial period

characterized by high $\delta^{18}O$. Sediment supply rates from the Tian Shan would be expected to be lower during interglacial than during glacial periods.

6. Conclusion

[72] Our study of two well imaged active folds, the Yakeng and Quilitak anticlines, provides a number of new techniques and concepts for quantitative interpretation of active folding of the land surface. Nevertheless we have not addressed the full range of known large-scale upper crustal folding mechanisms but have restricted ourselves to two contrasting mechanisms in adjacent folds that share a common shortening history: detachment folding (Yakeng) and fault bend folding (Quilitak). Other important folding mechanisms such as shear fault bend folding and classical and trishear fault propagation folding will predict different surface expressions of instantaneous fold kinematics. Nevertheless our study shows that the subsurface folding kinematics is the key issue for deciphering the folding of active landscapes. For both our examples, active distortion at the surface directly reflects the underlying folding kinematics as long as uplift rates are greater than sedimentation rates. The principal parameter for understanding and interpreting thrust-related morphology is the distribution of instantaneous uplift relative to total uplift.

[73] Our first example, the Yakeng detachment fold, is shown to grow in a self-similar fashion, with the surface morphology coinciding with the finite fold structure and having the same shape but at reduced amplitude. Landscape warping associated with this type of folding can be easily interpreted, and folded sedimentary markers such as terraces can be directly used to compute the amount of folding since deposition, and thus the shortening rate. This detachment fold strongly contrasts with fault bend folds like Quilitak in which active deformation occurs only along active axial surfaces that are pinned to fault bends and bound regions of different underlying fault dips. The abrupt transition in uplift rate across active axial surfaces produces fold scarps at the land surface. The Quilitak topographic front is a striking example, showing 600- to 700-m-high cumulative fold scarps with a distinctive triangular facet morphology. At a smaller scale these active axial surfaces are seen to have finite widths on the order of 25–150 m, which lead to complex bed-by-bed interactions between deformation and sedimentation and erosion that can be effectively modeled using a self-similar curved hinge kink band migration model. This type of model can be used further to directly fit field data on bed and fold scarp shapes to quantitatively estimate displacement rates on the underlying fault.

[74] Our study of active folding in the Kuche area of the southern Tian Shan has also given constraints on the long-term deformation rates, which turn out to be rather surprising. The primary observations have been deformation rates relative to sedimentation rates, which have then been approximately calibrated to the magnetostratigraphy of *Charreau et al.* [2006]. Yakeng in particular shows a nearly constant shortening rate of only ~0.16 mm/yr from 5.5 Ma to ~0.2–0.3 Ma at which point there was an order-of-magnitude acceleration of shortening rate which led to the topographic emergence of Yakeng anticline. A similar topographic emergence and acceleration of deformation is observed for the Quilitak anticline, such that the combined long-term shortening rate for these two structures at the southern edge of the Tian Shan has accelerated by approximately an order of magnitude from ~0.6 to ~4–5 mm/yr. This acceleration may have a straightforward local cause involving a concurrent turning off of shortening in the northern part of the Kuche thrust belt, which is largely inactive at present. Alternatively, there may have been an overall acceleration of deformation in the southern Tian Shan or in the Tian Shan as a whole [e.g., *Abdrakhmatov et al.*, 1996; *Burchfiel et al.*, 1999; *Burbank et al.*, 1999; *Zheng et al.*, 2000]. Thus the underlying tectonic scope and cause of this acceleration is unknown at present.

Appendix A: Strike and Dip Data Derived From Stereoscopic Corona Images

[75] The bedding attitude measurements shown in Figures 14, 16, 17, and 21 were extracted from Corona satellite images using the Stereo Program developed by *Bilotti et al.* [2000]. The methods described below.

[76] Corona images are satellite reconnaissance photographic images developed by the U.S. government during the Cold War with a ground resolution of 6 to 3 m per pixel and with stereoscopic capacity [*McDonald*, 1997; *Campbell*, 2002]. The images were available originally on 70 mm film and now in digital format without any geographic reference frame. We georeferenced and rectified and the Corona images using ground control points and Landsat and Spot images. During this rectification process we first decreased the resolution of the Corona images to values comparable to the georeferenced Landsat and Spot images. We then obtained low-resolution georeferenced Corona images. In a second step, we applied this rectification to the full resolution Corona images with maximum error below 2.5%.

[77] *Bilotti et al.* [2000] have developed a numerical method for measuring the strike and dip of bedding using stereoscopic pairs of images without rigorous photogrammetric parameters. Strike and dip measurements are obtained by mapping the bedding contact across topography at 3 points of different elevation. The Stereo Program was successfully applied to Landsat TM and Spot images, and to aerial photographs by *Bilotti et al.* [2000]. Here we apply the technique for the first time to Corona images in the Kuche belt to obtain strike and dip data in key inaccessible locations.

[78] To check the accuracy of measured strike and dip using stereo Corona images, we compared ground strike and dip data measured in the field in the Kuche thrust belt with the strike and dip data obtained with the Stereo Program. A total of 140 points are compared. Strike values were consistent in both data sets with an error less than ±2°. Dip values show larger variations reaching a maximum value of ±4° (Figure A1). Statistical analysis shows that the dip data have a standard deviation of 2.8 and variance of 6.7 for all points. We further observe that in zones with low topographic relief and without visible stratigraphic contrast, errors associated with dip measurements rapidly increase to more than 10°. In contrast, in zones with high stratigraphic contrast and moderate to high topographic relief dip errors are ±4°. The technique is still acceptable in flat areas with

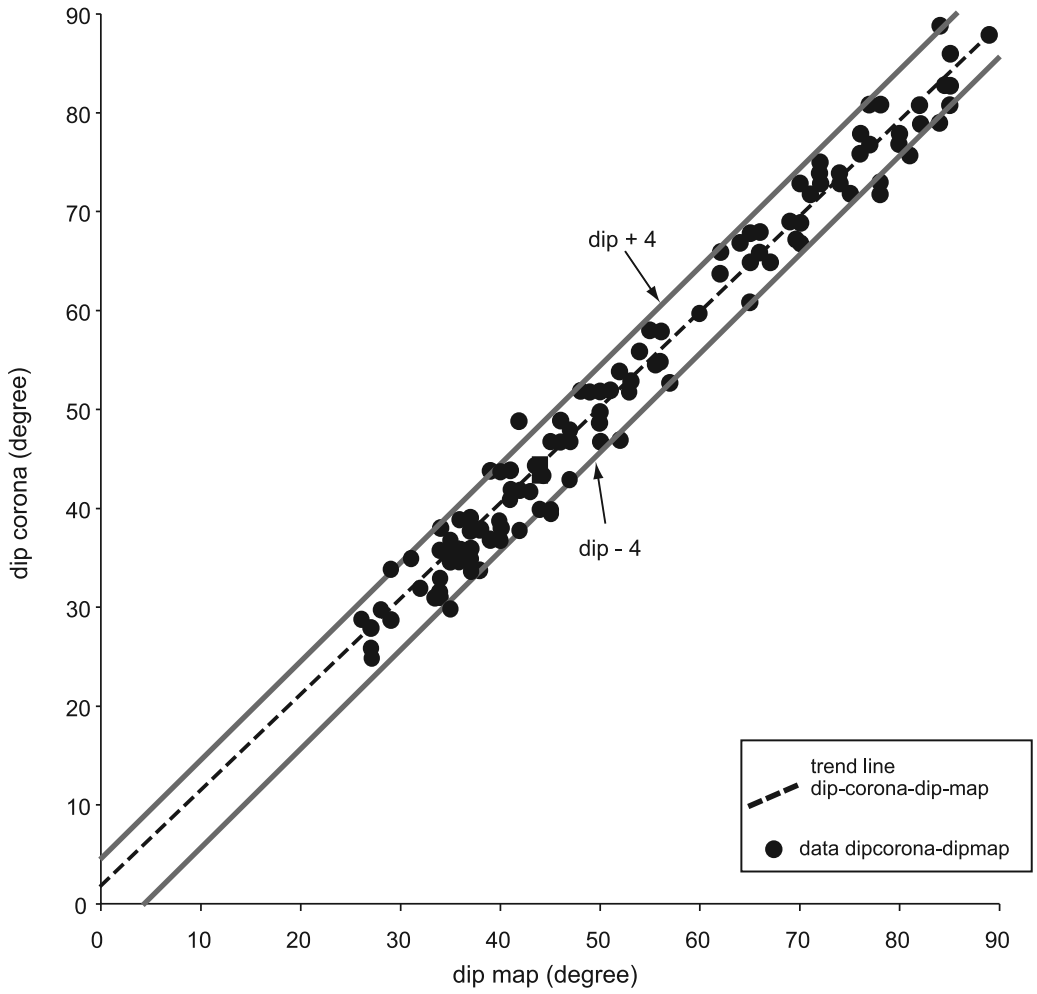

Figure A1. Field test of dip determination from Corona satellite images. The graph compares data from outcrop measurements strike and dip in the Kuche belt with measurements obtained with the Stereo Program from Corona images in the same locations.

low dipping visually well contrasting beds, even if dip errors reach ±7°. We conclude that it is possible to obtain reliable strike and dip data using stereo Corona images in mountainous areas where fieldwork is physically and logistically impracticable or impossible.

[79] **Acknowledgments.** This study was supported by NSF EAR-0073759, NSFC 49832040, TPEDB-PetroChina, Princeton 3-D Structure Project, and the Swiss National Science Foundation (SNSF 20020-101781). We particularly thank PetroChina for logistic organization in the field and for giving us access to seismic reflection profiles, well data, and magnetostratigraphic data. Jean-Phillipe Avouac, Stephan Dominguez, and Karl Mueller are warmly thanked for their constructive and useful reviews. Julien Charreau has been really helpful in providing us details about his magnetostratigraphic study.

References

Abdrakhmatov, K. Y., et al. (1996), Relatively recent construction of the Tian Shan inferred from GPS measurements of the present-day crustal deformation rates, *Nature*, *384*, 450–452.

Allen, M. B., S. J. Vincent, and P. J. Wheeler (1999), Late Cenozoic tectonics of the Kepingtage thrust zone: Interaction between the Tien Shan and the Tarim Basin, northwest China, *Tectonics*, *18*, 639–654.

Allmendinger, R. W. (1998), Inverse and forward numerical modeling of trishear fault-propagation folds, *Tectonics*, *17*, 640–656.

Armijo, R., P. Tapponnier, J. L. Mercier, and H. Tonglin (1986), Quaternary extension in southern Tibet, *J. Geophys. Res.*, *91*, 13,803–13,872.

Avouac, J. P., P. Tapponnier, M. Bai, H. You, and G. Wang (1993), Active thrusting and folding along the northern Tian Shan and late Cenozoic rotation of the Tarim relative to Dzungaria and Kazakhstan, *J. Geophys. Res.*, *98*, 6755–6804.

Bilotti, F., J. Shaw, and P. Bernnan (2000), Quantitative structural analysis with stereoscopic remote sensing imagery, *AAPG Bull.*, *84*, 727–740.

Burbank, D. W., J. Leland, E. Fielding, R. S. Anderson, N. Brozovic, M. R. Reid, and C. Duncan (1996a), Bedrock incision, rock uplift and threshold hillslopes in the northwestern Himalayas, *Nature*, *379*, 505–510.

Burbank, D., A. Meigs, and N. Brozovic (1996b), Interactions of growing folds and coeval depositional systems, *Basin Res.*, *8*, 199–223.

Burbank, D. W., J. K. Mclean, M. Bullen, K. Y. Abdrakhmatov, and M. M. Miller (1999), Partitioning of the intermontane basins by thrust-related folding, Tien Shan, Kyrgystan, *Basin Res.*, *11*, 75–92.

Burchfiel, B. C., E. T. Brown, Q. Deng, F. Xianyue, L. Jun, P. Molnar, J. B. Shi, Z. Wu, and H. C. You (1999), Crustal shortening on the margins of the Tien Shan, Xianjiang, China, *Int. Geol. Rev.*, *41*, 665–700.

Campbell, J. (2002), *Introduction to Remote Sensing*, 621 pp., Guilford, New York.

Charreau, J., S. Gilder, Y. Chen, S. Dominguez, J.-P. Avouac, S. Sen, M. Jolivet, Y. Li, and W. Wang (2006), Magnetostratigraphy of the Yaha section, Tarim Basin (China): 11 Ma acceleration in erosion and uplift of the Tian Shan mountains, *Geology*, *34*, 181–184.

Chen, J., D. W. Burbank, K. M. Scharer, E. Sobel, J. Yin, C. Rubin, and R. Zhao (2002), Magnetochronology of the Upper Cenozoic strata in the southern Chinese Tian Shan: Rates of Pleistocene folding and thrusting, *Earth Planet. Sci. Lett.*, *195*, 113–130.

Dittmann, S. T. (2005), Investigating detachment fold shortening in the Yakeng Anticline, China: An area relief and surface analysis, Bachelor thesis, 40 pp., Princeton Univ., Princeton, N. J.

Epard, J.-L., and R. H. Groshong (1995), Kinematic model of detachment folding including limb rotation, fixed hinges, and layer-parallel strain, *Tectonophysics*, *247*, 85–103.

Erslev, E. A. (1991), Trishear fault-propagation folding, *Geology*, *19*, 617–620.

Gonzalez-Mieres, R., and J. Suppe (2006), Relief and shortening in detachment folds, *J. Struct. Geol.*, *28*(10), 1785–1807, doi:10.1016/j.jsg.2006.07.001.

Guan, S. (2004), Geometric and kinematic analysis of late Cenozoic fold-and-thrust belt in Kuche and Kashi area, southern Tian Shan (in Chinese with English abstract), Ph.D. thesis, 136 pp., Dep. of Geosci., Zhejiang Univ., Hangzhou, China.

Hardy, S., and M. Ford (1997), Numerical modelling of trishear fault-propagation folding, *Tectonics*, *16*(5), 841–854.

Holbrook, J., and S. A. Schumm (1999), Geomorphic and sedimentary response of rivers to tectonic deformation: A brief review and critique of a tool for recognizing subtle epeirogenic deformation in modern and ancient setting, *Tectonophysics*, *305*, 287–306.

Howard, A. D., and G. Kerby (1983), Channel changes in badlands, *Geol. Soc. Am. Bull.*, *94*, 739–752.

Howard, A. D., W. E. Dietrich, and M. A. Seidl (1994), Modeling fluvial erosion on regional to continental scales, *J. Geophys. Res.*, *99*, 13,971–13,986.

Hubert-Ferrari, A., J. Suppe, X. Wang, and C. Z. Jia (2005a), Yakeng detachment fold, south Tian Shan, China, in *Seismic Interpretation of Contractional Fault-related Folds*, *Seismic Atlas*, edited by J. Shaw, C. Connors, and J. Suppe, 110–113, Am. Assoc. Pet. Geol., Tulsa, Okla.

Hubert-Ferrari, A., J. Suppe, J. Van Der Woerd, X. Wang, and H. Lu (2005b), Irregular earthquake cycle along the southern Tian Shan front, Aksu area, China, *J. Geophys. Res.*, *110*, B06402, doi:10.1029/2003JB002603.

Humphrey, N. F., and S. K. Konrad (2000), River incision or diversion in response to bedrock uplift, *Geology*, *28*, 43–46.

Hutrez, J.-E., F. Lucazeau, J. Lavé, and J.-P. Avouac (1999), Investigation of the relationships between basin morphology, tectonic uplift, and denudation from the study of an active fold belt in the Siwalik Hills, central Nepal, *J. Geophys. Res.*, *104*, 12,779–12,796.

Imbrie, J., J. D. Hays, A. McIntyre, A. C. Mix, J. J. Morley, N. G. Pisias, W. L. Prell, and N. G. Shackleton (1984), The orbital theory of Pleistocene climate: Support from a revised chronology of the marine δ^{18}O record, in *Milankovitch and Climate, Part 1*, edited by A. Berger et al., pp. 269–305, Springer, New York.

Ishiyama, T., K. Mueller, M. Togo, A. Okada, and K. Takemura (2004), Geomorphology, kinematic history, and earthquake behavior of the active Kuwana wedge thrust anticline, central Japan, *J. Geophys. Res.*, *109*, B12408, doi:10.1029/2003JB002547.

Koons, P. O. (1989), The topographic evolution of collisional mountain belts: A numerical look at the southern Alps, New Zealand, *Am. J. Sci.*, *289*, 1041–1069.

Lavé, J., and J. P. Avouac (2000), Active folding of fluvial terraces across the Siwalik Hills (Himalaya of central Nepal), *J. Geophys. Res.*, *105*, 5735–5770.

McDonald, R. (1997), Corona, Argon, and Landyard: A revolution for US overhead reconnaissance, in *Corona Between the Sun and the Earth, the First NRO Reconnaissance Eye in the Space*, edited by R. McDonald, 61–74, Am. Soc. for Photogramm. and Remote Sens., Bethesda, Md.

Medwedeff, D. A. (1992), Geometry and kinematics of an active, laterally propagating wedge thrust, Wheeler Ridge, California, in *Structural Geology of Fold and Thrust Belts*, edited by S. Mitra and G. W. Fisher, pp. 2–28, Johns Hopkins Univ. Press, Baltimore, Md.

Molnar, P., and Q. Deng (1984), Faulting associated with large earthquakes and the average rate of deformation in central and eastern Asia, *J. Geophys. Res.*, *89*, 6203–6227.

Molnar, P., and S. Ghose (2000), Seismic moments of major earthquakes and the rate of shortening across Tien Shan, *Geophys. Res. Lett.*, *27*, 2377–2380.

Molnar, P., and P. Tapponnier (1975), Cenozoic tectonics of Asia: Effects on a continental collision, *Science*, *189*, 419–426.

Mueller, K., and P. Tailing (1997), Geomorphic evidence for tear faults accommodating lateral propagation of an active fault-bend fold, Wheeler Ridge, California, *J. Struct. Geol.*, *19*, 397–411.

Ouchi, S. (1985), Response of alluvial rivers to slow active tectonic movement, *Geol. Soc. Am. Bull.*, *96*, 504–515.

Poblet, J., and K. McClay (1996), Geometry and kinematics of single-layer detachment folds, *AAPG Bull.*, *80*, 1085–1109.

Poblet, J., K. McClay, F. Storti, and J. A. Munoz (1997), Geometries of syntectonic sediments associated with single layer detachment folds, *J. Struct. Geol.*, *19*, 369–381.

Poisson, B., and J. P. Avouac (2004), Holocene hydrological changes inferred from alluvial stream entrenchment in North Tian Shan (northwestern China), *J. Geol.*, *112*, 231–249.

Reigber, Ch., G. W. Michel, R. Galas, D. Angermann, J. Klotz, J. Y. Chen, A. Papschev, R. Arslanov, V. E. Tzurkov, and M. C. Ishanov (2001), New space geodetic constraints on the distribution of deformation in central Asia, *Earth Planet. Sci. Lett.*, *191*, 157–165.

Shaw, J., and J. Suppe (1994), Active faulting and growth folding in the eastern Santa Barbara Channel, California, *Geol. Soc. Am. Bull.*, *106*, 607–626.

Shaw, J., S. C. Hook, and J. Suppe (1994), Structural trend analysis by axial surface mapping, *AAPG Bull.*, *78*, 700–721.

Shaw, J., C. Connors, and J. Suppe (2005), Part 1: Structural interpretation methods, in *Seismic Interpretation of Contractional Fault-Related Folds*, *Seismic Atlas*, edited by J. Shaw, C. Connors, and J. Suppe, pp. 1–58, Am. Assoc. of Pet. Geol., Tulsa, Okla.

Shaw, J. H., A. Plesch, J. F. Dolan, T. L. Pratt, and P. Fiore (2002), Puente Hills blind-thrust system, Los Angeles, California, *Bull. Seismol. Soc. Am.*, *92*, 2946–2960.

Sun, Z., X. Feng, D. Li, F. Yang, Y. Qu, and H. Wang (1999), Cenozoic Ostracoda and palaeoenvironments of the northeastern Tarim basin, western China, *Palaeogeogr. Palaeoclimatol. Palaeoecol.*, *148*, 37–50.

Suppe, J. (1983), Geometry and kinematics of fault-bend folding, *Am. J. Sci.*, *283*, 684–721.

Suppe, J. (2006), Mass balance and thrusting in detachment folds, in *Thrust-Related Folding*, edited by K. McClay, J. H. Shaw, and J. Suppe, *AAPG Mem.*, submitted.

Suppe, J., G. T. Chou, and S. C. Hook (1992), Rate of folding and faulting determined from growth strata, in *Thrust Tectonics*, edited by K. McClay, pp. 105–122, CRC Press, Boca Raton, Fla.

Suppe, J., F. Sabat, J. A. Muños, J. Poblet, E. Roca, and J. Verges (1997), Bed-by-bed fold growth by kink-band migration: Sant Llorenç de Morunys, eastern Pyrenees, *J. Struct. Geol.*, *19*, 443–461.

Suppe, J., C. Connors, and Y. Zhang (2004), Shear fault-bend folding, in *Thrust Tectonics and Hydrocarbon Systems*, edited by K. McClay, *AAPG Mem.*, 82, 303–323.

Süss, M. P., and J. H. Shaw (2003), *P* wave seismic velocity structure derived from sonic logs and industry reflection data in the Los Angeles basin, California, *J. Geophys. Res.*, *108*(B3), 2170, doi:10.1029/2001JB001628.

Tapponnier, P., and P. Molnar (1979), Active faulting and Cenozoic tectonics of the Tien Shan, Mongolia and Baykal regions, *J. Geophys. Res.*, *84*, 3425–3459.

Thompson, S. C., R. J. Weldon, C. M. Rubin, K. Abdrakhmatov, P. Molnar, and G. W. Berger (2002), Late Quaternary slip rates across the central Tien Shan, Kyrgyzstan, central Asia, *J. Geophys. Res.*, *107*(B9), 2203, doi:10.1029/2001JB000596.

Wang, Q., et al. (2001), Present-day crustal deformation in China constrained by global positioning system measurements, *Science*, *294*, 574–577.

Yin, A., S. Nie, P. Craig, T. M. Harrison, F. T. Ryerson, X. Qian, and G. Yang (1998), Late Cenozoic tectonic evolution of the southern Chinese Tian Shan, *Tectonics*, *17*, 1–27.

Yue, L. F., J. Suppe, and J. H. Hung (2005), Structural geology of a classic thrust belt earthquake: The 1999 Chi-Chi earthquake Taiwan (M_w = 7.6), *J. Struct. Geol.*, *27*, 2058–2083.

Zheng, H., C. Powell, Z. An, J. Zhou, and G. Dong (2000), Pliocene uplift of the northern Tibetan Plateau, *Geology*, *28*, 715–718.

R. Gonzalez-Mieres and J. Suppe, Department of Geosciences, Princeton University, Princeton, NJ 08544, USA.

A. Hubert-Ferrari, Royal Observatory of Belgium, Av. de la Circulaire 3, Brussels B-1180, Belgium. (aurelia.ferrari@oma.be)

X. Wang, Geosciences Department, Zhejiang University, Hangzhou, China 310027.